Electronic Tuning of Electrocatalytic CO_2 Reduction Using Tetradentate Cobalt Aminopyridine Complexes

Milaş Dan

Master Thesis (TFM)

July 2024

Supervised by Prof. Julio Lloret-Fillol

Contents

1. Introduction

The driver of climate change are the anthropogenic CO_2 emissions which, as a weak acid, can also quickly cause ocean acidification.[1] As global CO_2 emission levels are on a steady increase,[2] reaching 35.8 Gt of CO_2 emitted in 2023,[3] it is imperative to find ways to capture and utilize CO_2 in a productive manner.

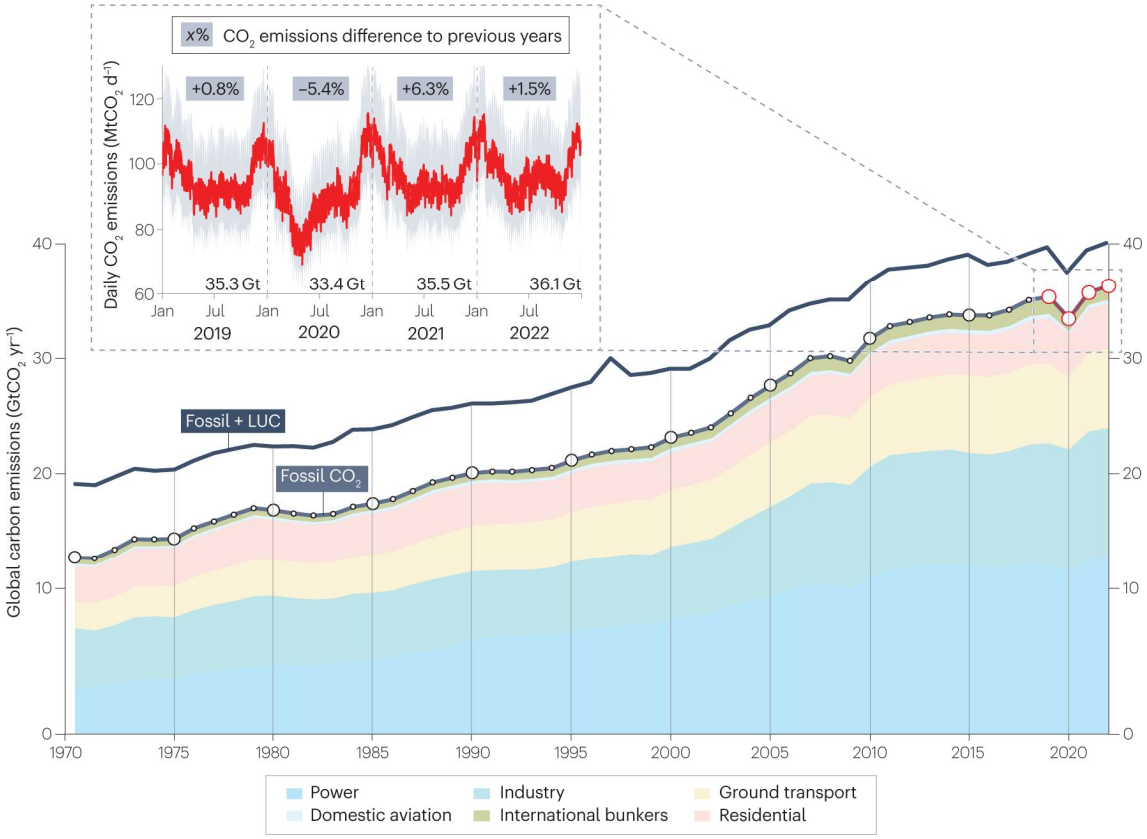

Figure 1. Global CO_2 emissions 1970–2022 showing steady increase, with a brief reduction during the 2020 COVID pandemic and resuming course immediately after. Reprinted (adapted) with permission from {*Nat Rev Earth Environ* 4, 205–206 (2023)}. Copyright {2023} Nature Reviews Earth & Environment.[2]

With the significant development and growth of the renewable energy industry, especially solar and wind,[4] the potential to convert human-made CO_2 emissions into valuable chemicals and fuels via catalytic electroreduction has the potential to alleviate our dependence on fossil fuels[5,6] and the impact of climate change. While it offers a potentially effective way to reduce greenhouse gas emissions this technique is suffering

from certain drawbacks, such as electrode instability, large overpotentials, low Faraday efficiencies, competition with reduction processes taking place at a similar potential (hydrogen evolution), and selectivity for the desired products.[7] Among catalysts for CO_2 electrocatalysis based on noble-metal (such as Au, Ag, and Pd) have been used with great success because they offer strong electrocatalytic performances, selectivity, and stability with minimal overpotential.[8] However, their high cost has limited their applications. On the other hand, earth-abundant 3d metals are suffering from other drawbacks such as low turnover numbers (TON) and Faraday efficiency (FE). Due to their high tunability, molecular metal complexes offer a particularly interesting avenue to better understand the underlying catalytic mechanisms of CO_2 reduction to later design and obtain inexpensive, highly active, efficient and selective catalysts.

Cobalt complexes have been very active for the CO_2 reduction reaction (CO_2RR). The reduction of CO_2 to CO has been reported for porphyrin, phthalocyanine and aminopyridine complexes. Co^{II} tripodal complexes[9] (FE 60%, TON_{300min} 5), Co quaterpyridine complexes[10] (FE 94%, TON_{180min} 17), Co terpyridine complexes[11] (FE 12%, $TON_{180min} < 1$).[12–14] While the performance of these Co complexes in the reduction of CO_2 to CO is varied, the mechanistic understanding of their catalytic behavior can serve benefit the research community to provide insight on how to overcome current barriers towards more active and selective systems.

Cobalt complexes containing tetradentate aminopyridyl ligands are interesting homogeneous catalyst for CO_2 reduction.[7,15] A recently published study[15] from the hosting research group has shed light on the mechanistic process for one such example of aminopyridine cobalt complex with the ligand 1-[2-pyridylmethyl]-4,7-dimethyl-1,4,7-triazacyclononane, in both electro- and photocatalytic CO_2 reduction to CO (**Figure 2**). In the publication, authors showed that *in-situ* generated Co^{I} species is nucleophilic enough to bind CO_2 and that the C-O bond can be cleaved to produce CO under mild conditions (room temperature, reasonably low potentials) in CH_3CN.

Authors also showed that under electrochemical conditions the reduction of $Co^{II/I}$ to Co^{I} by the electrode eclipses the release of CO leading to an accumulation of Co^{I}-CO (limiting step), at which point the catalysis can only proceed through a low-valence $Co^{I/0}$

species (Figure 2, right side), a bimolecular process, and ultimately leads to lower TON. However, under blue light irradiation at a constant potential of -2.46 V held for 6 h, a substantial catalytic improvement of the Co^{II} species in terms of FE and TON is observed compared to the experiments without irradiation. This observation was in agreement with the beneficial effect of blue light on electrocatalysis due to the light-induced cleavage of some of the constantly accumulating Co^{I}-CO stable species responsible for the interruption of the catalytic cycle (not allowing the catalyst to regenerate). The experiment was repeated at a more positive potential, however, produced barely observable effect, suggesting a smaller impact of light on the Co^{I}-CO species at this potential.

Authors concluded that the electrocatalytic reduction of CO_2 to CO by the cobalt complex is inhibited by the constant accumulation of the stable Co^{I}-CO species in solution, but under light irradiation the constant cleaving of the Co^{I}-CO bond with the release of CO allows the catalyst to regenerate and continue the catalytic process, leading to higher FE and TON values.

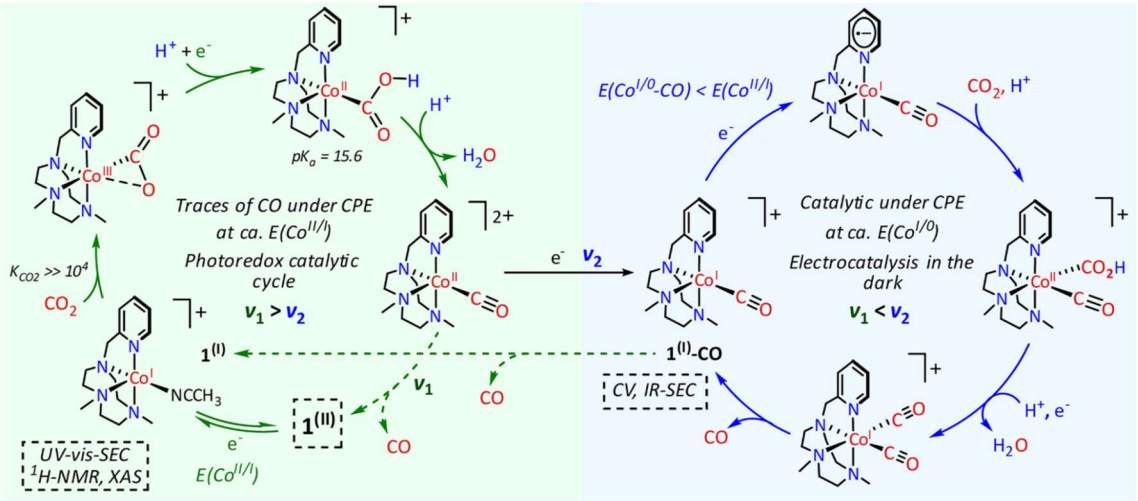

Figure 2. Proposed electro- and photo-catalytic CO_2 reduction to CO mechanism by Julio Lloret-Fillol *et al.*[15] Reprinted (adapted) with permission from {*Inorg. Chem.* 2014, 53, 10, 4980–4988}. Copyright {2020} American Chemical Society.

In this work, we have set to explore the effects of 4 electronic-donating or electronic-withdrawing groups (hydrogen, cyan, ester and dimethyl methoxy) in the electro-

catalytical reduction of CO_2 to CO by the same cobalt complex, under dark and under light irradiation.

2. Objectives

- Synthetize cobalt complexes **Co(Py$^{(H,H)}$Me$_2$tacn)**, **Co(Py$^{(CN,H)}$Me$_2$tacn)**, **Co(Py$^{(COOEt,H)}$Me$_2$tacn)** and **Co(Py$^{(OMe,Me)}$Me$_2$tacn)** which have different electron-donating or electron-withdrawing substituents in the pyridine ring of the ligand.
- Study their performance in electrocatalytic CO_2 reduction through cyclic voltammetry (CV) and controlled-potential electrolysis (CPE).
- Study the effect of light on their catalysis performance through CV and CPE.

3. Results and discussion

3.1. Synthesis of ligands and complexes

The following four cobalt catalysts were synthesized and studied (**Figure 3**): **Co(Py$^{(H,H)}$Me$_2$tacn)**, **Co(Py$^{(CN,H)}$Me$_2$tacn)**, **Co(Py$^{(COOEt,H)}$Me$_2$tacn)** and **Co(Py$^{(OMe,Me)}$Me$_2$tacn).**

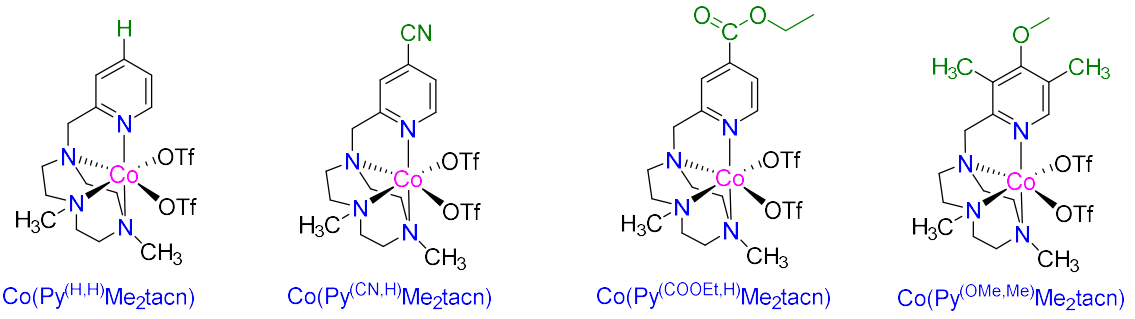

Figure 3. Tetradentate cobalt aminopyridine complexes synthesized and studied.

A general image of the steps taken for obtaining the four cobalt catalysts studied in this work can be seen in **Figure 4**:

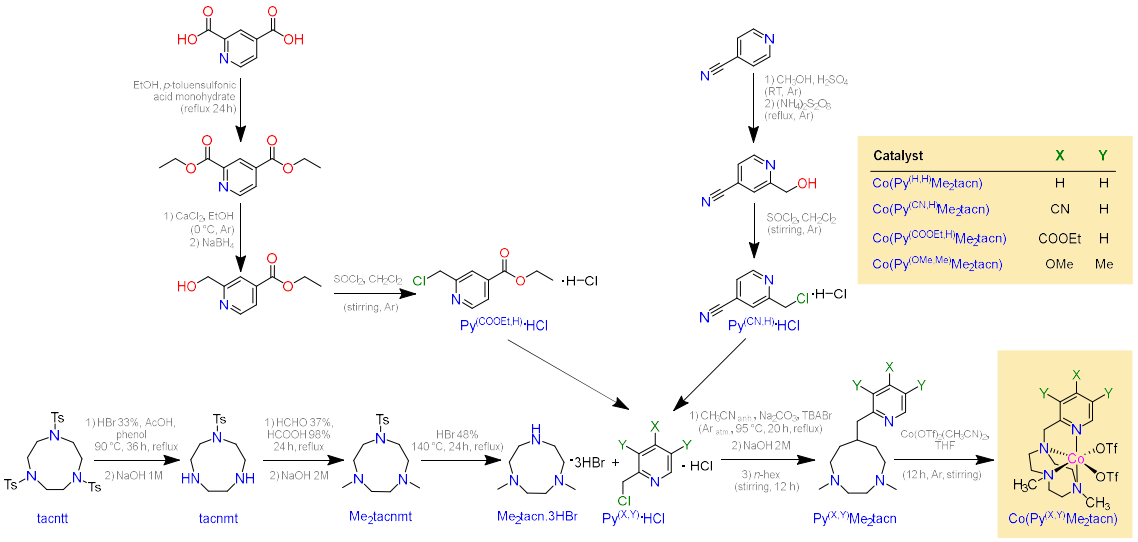

Figure 4. Overview of synthetic steps followed in this work.

Tetradentate nitrogen donating ligands have been synthesized by addition of 2-chloromethylpyridine (4 different substituents) to 1,4-dimethyl-1,4,7-triazonane hydrobromide (**Me_2tacn·3HBr**) as illustrated in **Figure 38**. The hydrogen and dimethyl methoxy chloromethylpyridine substrates ($Py^{(H,H)}Me_2tacn$·HCl and $Py^{(OMe,Me)}Me_2tacn$·HCl) were available from commercial sources, while the ester ligand **($Py^{(COOEt,H)}Me_2tacn$·HCl),** was synthesized starting from pyridine-2,4-dicarboxylic acid and the cyan (nitrile) ligand **($Py^{(CN,H)}Me_2tacn$·HCl)** starting from isonicotinonitrile.

Me_2tacn·3HBr was obtained in a 3-step synthetic process from 1,4,7-tritosyl-1,4,7-triazonane. In the first step we removed of two of the tosyl protecting groups by reflux with HBr 33% in acetic acid and phenol, to obtain **tacnmt**. In the ^{1}H-NMR **(Figure 5)** the signals are clearly visible except for the aminic protos N**H** (2H) which should appear around 1.85 ppm however due to traces of H_2O in the sample do not.

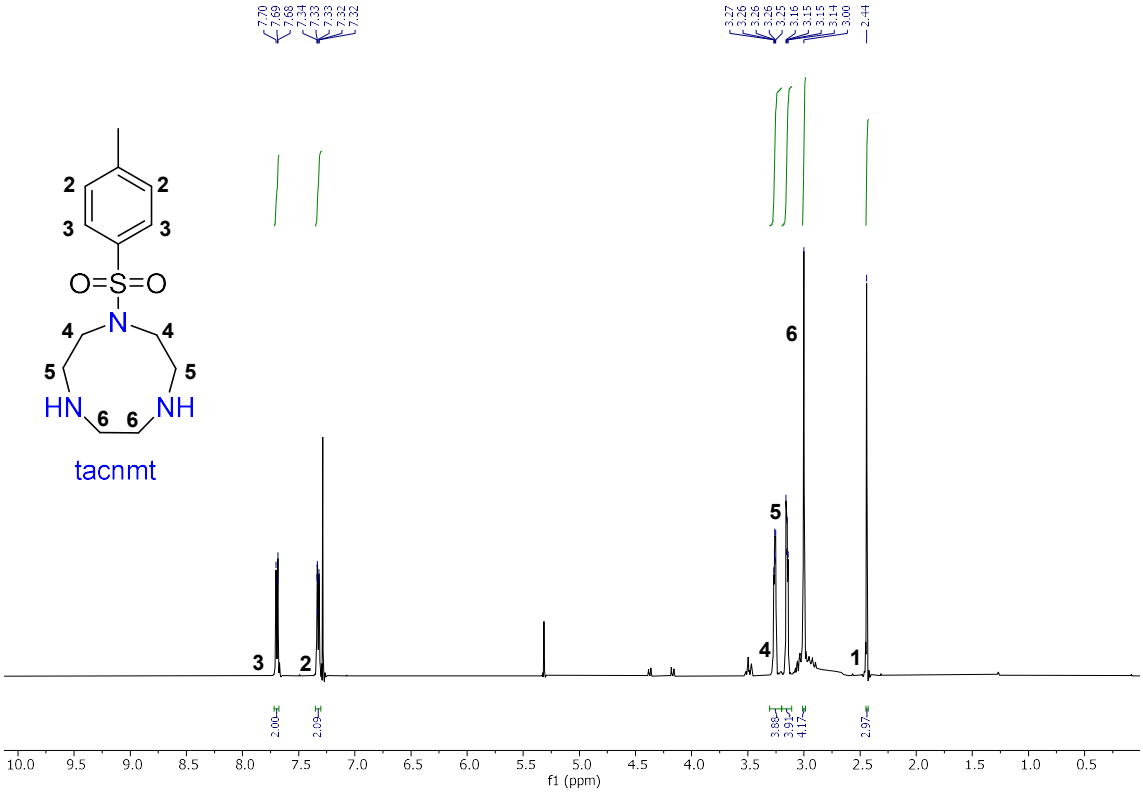

Figure 5. ^{1}H-NMR spectra of 1-tosyl-1,4,7-triazonane (**tacnmt**, $CDCl_3$, 500 MHz, 298 K).

Next, the methylation of the unprotected amino groups by refluxing with formic acid and formaldehyde provided **Me$_2$tacnmt**. The ^{1}H-NMR confirms the presence of the singlet peak corresponding to the two methyl groups that were added to the molecule **(Figure 6**, signal 7).

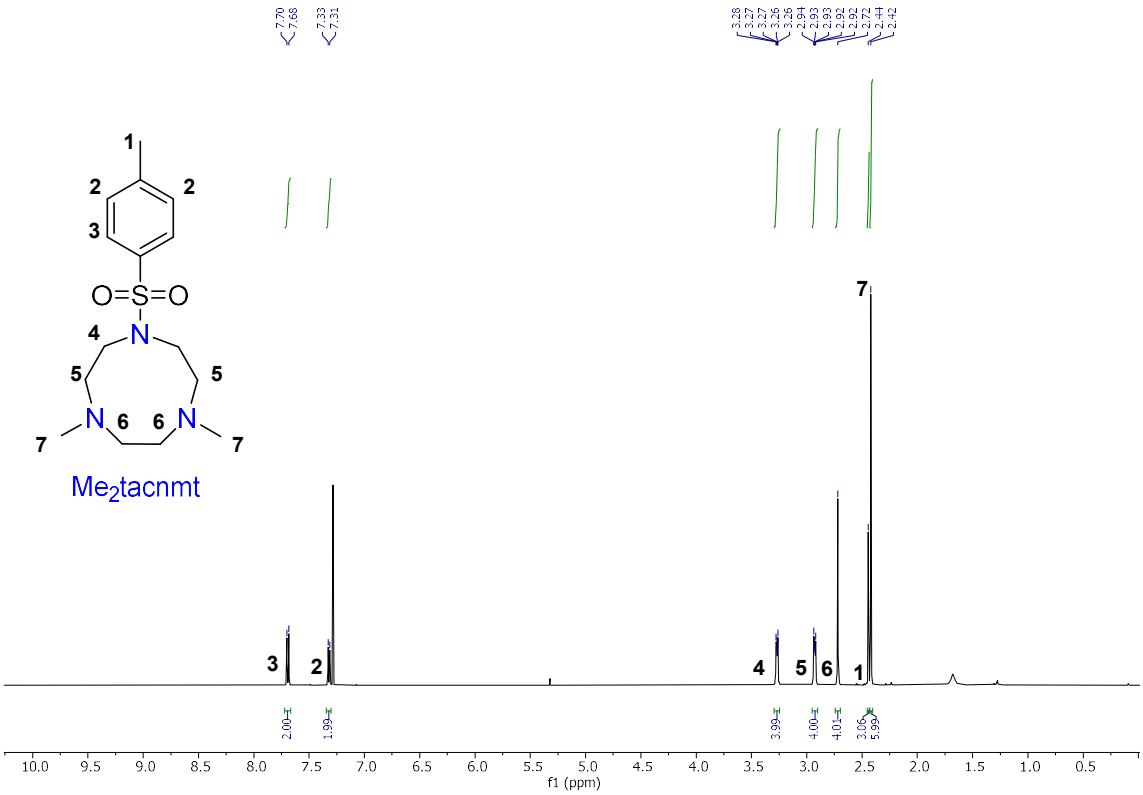

Figure 6. ^{1}H-NMR spectra of 1,4-dimethyl-7-tosyl-1,4,7-triazonane (**Me$_2$tacnmt**, $CDCl_3$, 500 MHz, 298 K).

In the last step we removed the last protective tosyl group by reflux with HBr 48%. The reaction displayed extreme sensitivity in the last step to the purity and concentration of the HBr. The ^{1}H-NMR shows the absence of signals in the aromatic region (**Figure 7**) but the aminic proton N**H** (1H) is once again not visible, this time because the NMR was recorded in deuterated water.

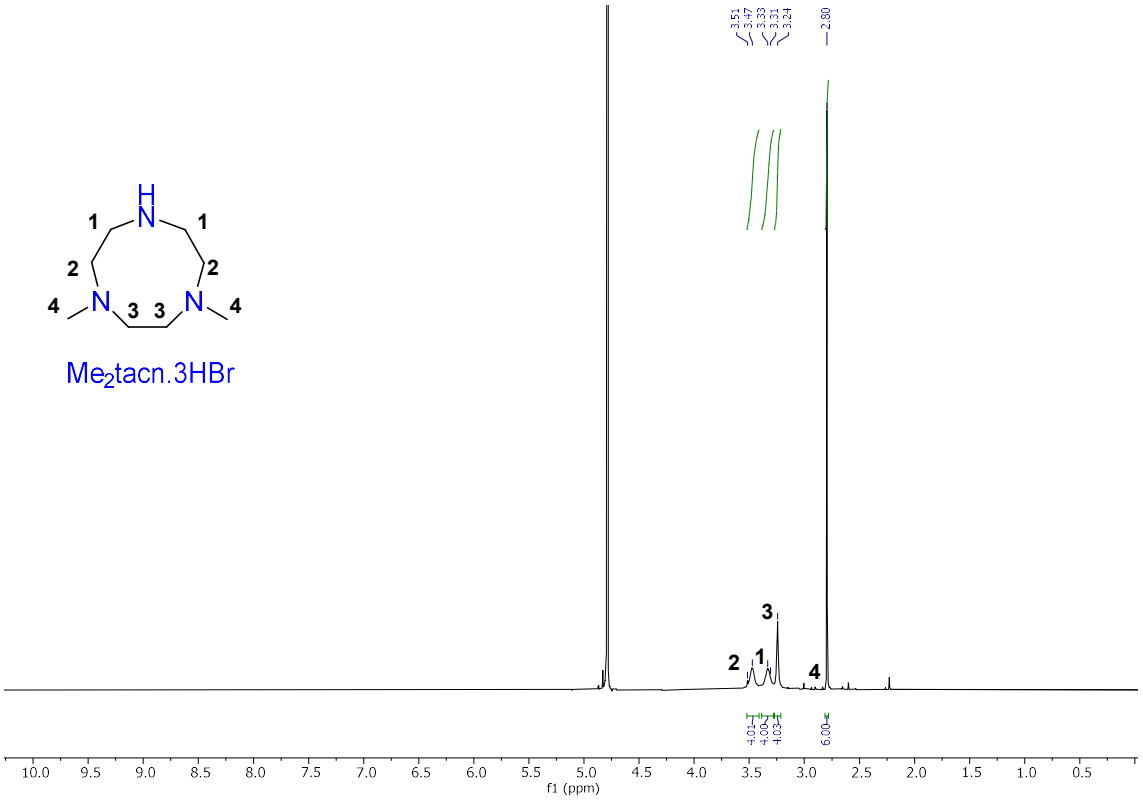

Figure 7. ^{1}H-NMR spectra of 1,4-dimethyl-1,4,7-triazonane trihydrobromide (**Me$_2$tacn·3HBr**, D_2O, 500 MHz, 298 K).

The ligands were obtained by alkylation under inert atmosphere of the appropriate 2-chloromethylpyridine to **Me$_2$tacn·3HBr**, using tetrabutylammonium bromide (TBABr), Na_2CO_3 and CH_3CN and refluxing for 20 hours.

Starting from commercially available 2-(chloromethyl)pyridine hydrochloride and the synthesized substrate **Me$_2$tacn·3HBr**, 1,4-dimethyl-7-(pyridin-2-ylmethyl)-1,4-diazonane (**Py$^{(H,H)}$Me$_2$tacn**) was obtained following the scheme in **Figure 8.**

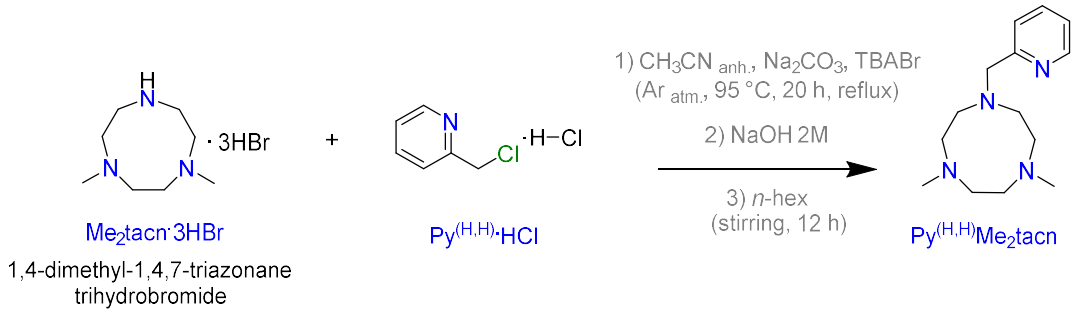

Figure 8. Synthetic scheme for the hydrogen ligand, 1,4-dimethyl-7-(pyridin-2-ylmethyl)-1,4,7-triazonane (**Py$^{(H,H)}$Me$_2$tacn**).

Ligand **Py$^{(H,H)}$Me$_2$tacn** displayed a clean ^{1}H-NMR spectrum, with the pyridinic protons visible in the aromatic region, and the dimethyl-triazocyclononane protons in the aliphatic region, as can be seen in **Figure 9**. Based on the lack of other signals a good purity of the compound can be assumed.

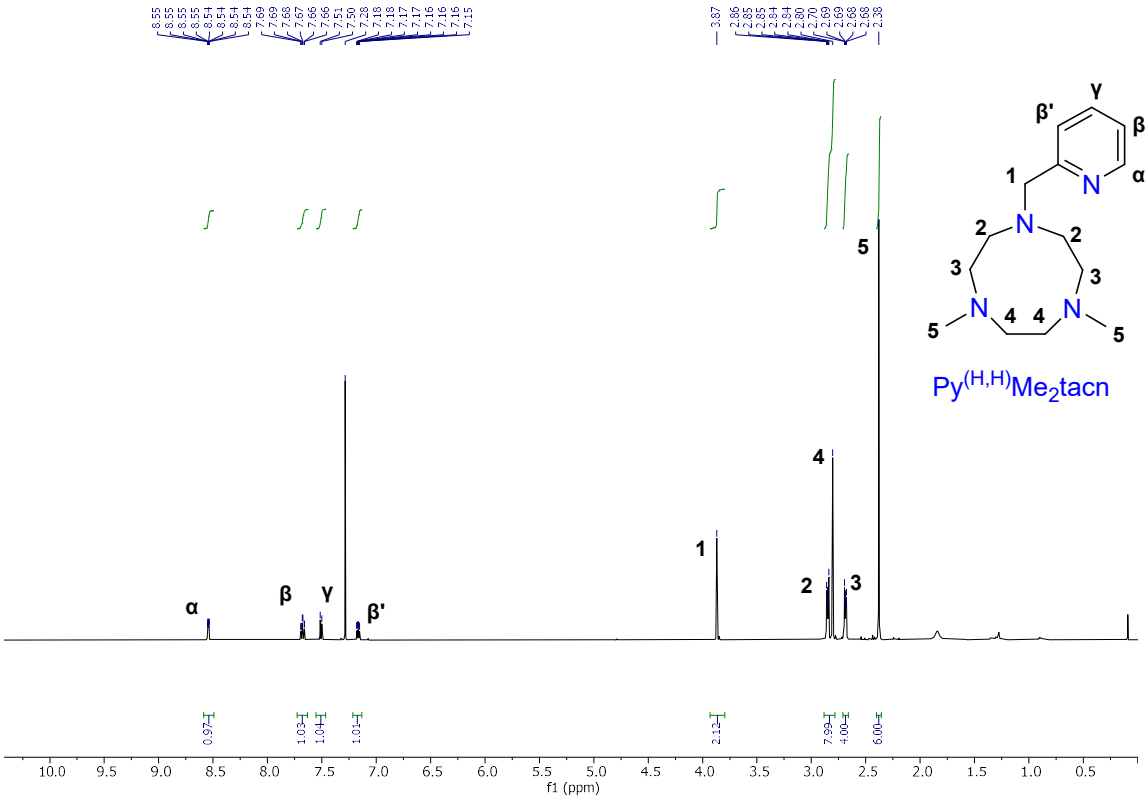

Figure 9. ^{1}H-NMR spectra of 1,4-dimethyl-7-(pyridin-2-ylmethyl)-1,4-diazonane (**Py$^{(H,H)}$Me$_2$tacn**, $CDCl_3$, 500 MHz, 298 K).

The ligand **Py$^{(CN,H)}$Me$_2$tacn** was obtained following the scheme in **Figure 10**, and described later in the experimental section.

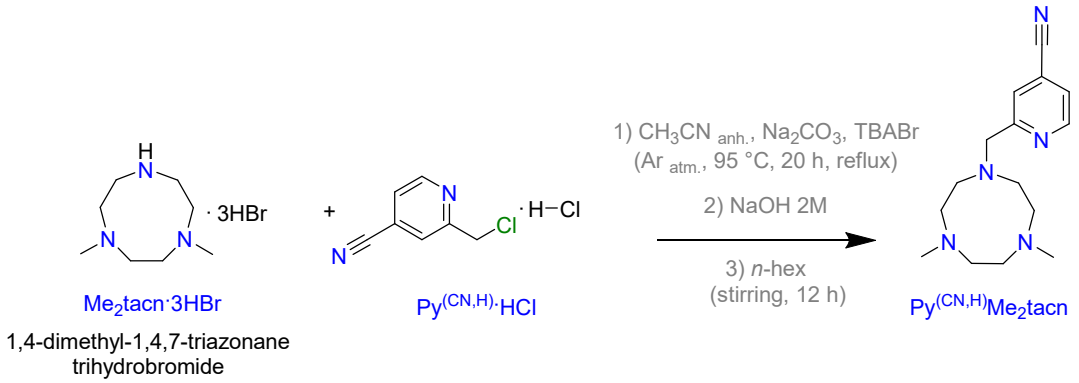

Figure 10. Synthetic scheme for **Py$^{(CN,H)}$Me$_2$tacn**, 2-((4,7-dimethyl-1,4,7-triazonan-1-yl)methyl)isonicotinonitrile.

The ^{1}H-NMR spectrum of this ligand **(Figure 11**) shows is similar to the previous ligand **(Py$^{(H,H)}$Me$_2$tacn)** and shows a clear absence of the γ-proton in the aromatic region**.**

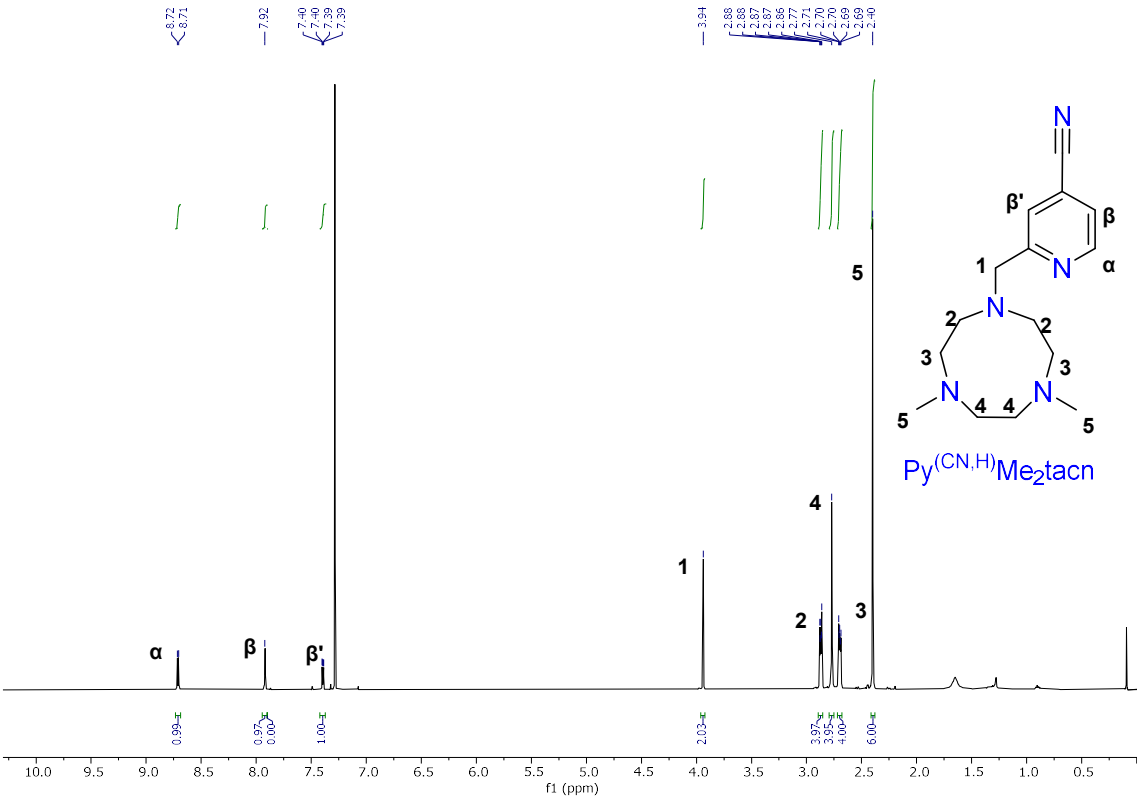

Figure 11. ^{1}H-NMR spectra of 2-((4,7-dimethyl-1,4,7-triazonan-1-yl)methyl)isonicotinonitrile (**Py$^{(CN,H)}$Me$_2$tacn**), $CDCl_3$, 500 MHz, 298 K).

The ester ligan, **Py$^{(COOEt,H)}$Me$_2$tacn**, followed a similar synthetic route (**Figure 12**).

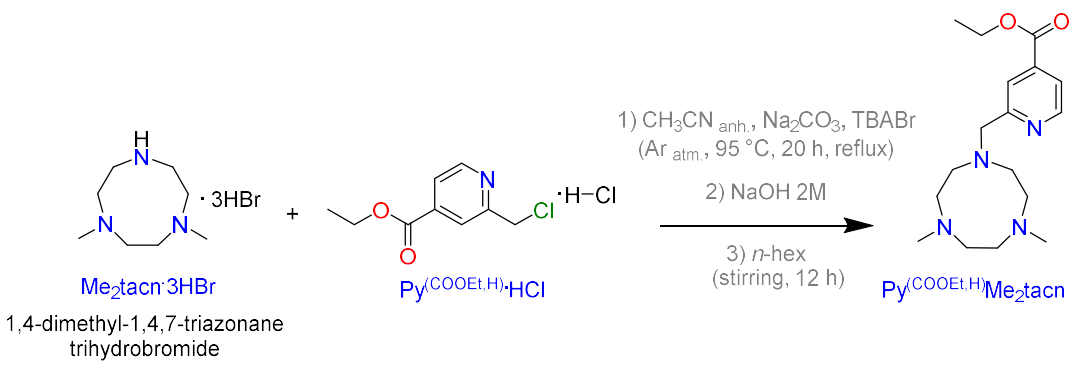

Figure 12. Synthetic scheme for the ester ligand, ethyl 2-((4,7-dimethyl-1,4,7-triazonan-1-yl)methyl)isonicotinate (**Py$^{(COOEt,H)}$Me$_2$tacn**).

The ^{1}H-NMR spectrum (**Figure 13**) shows distinctive signals for the ester moiety: (2H) at 4.43 ppm for CH$_3$-C**H$_2$**-OCO and (3H) at 1.44 for C**H$_3$**-CH$_2$-OCO.

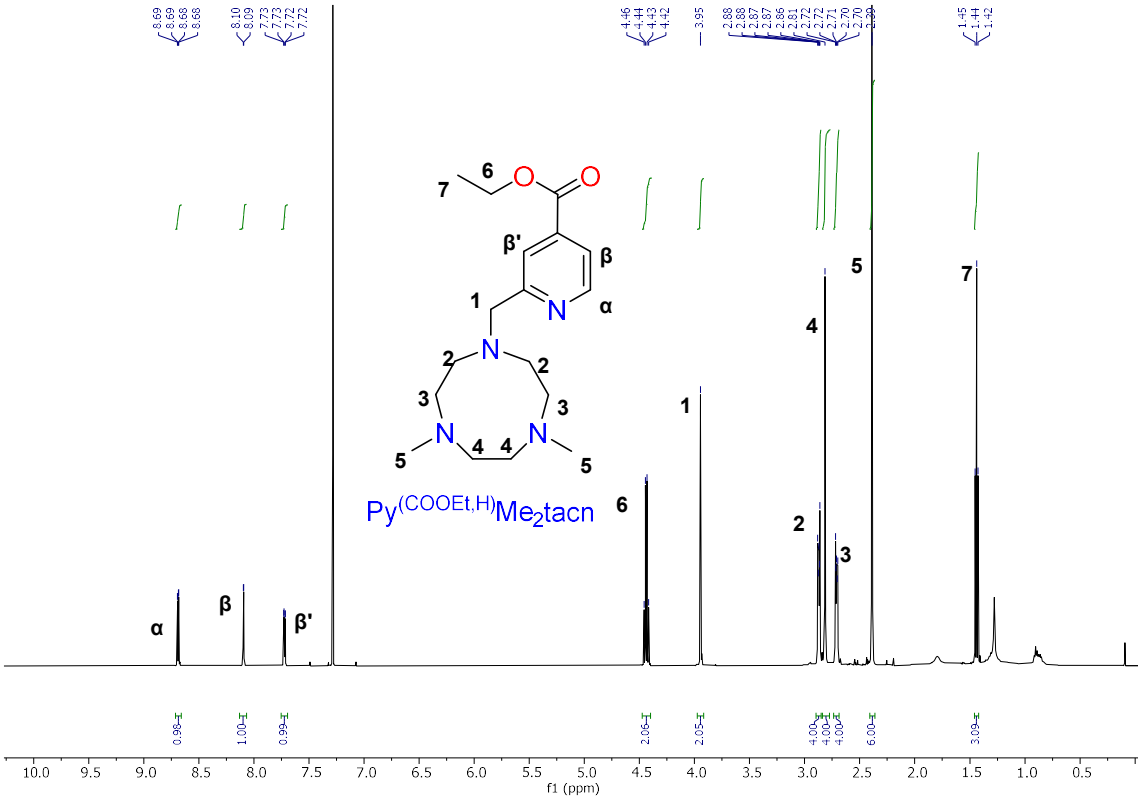

Figure 13. ^{1}H-NMR spectrum of ethyl 2-((4,7-dimethyl-1,4,7-triazonan-1-yl)methyl)isonicotinate (**Py$^{(COOEt,H)}$Me$_2$tacn**), CDCl$_3$, 500 MHz, 298 K).

Starting from commercially available 2-(chloromethyl)-4-methoxy-3,5-dimethylpyridine hydrochloride and previously synthesized **Me$_2$tacn·3HBr**, and similar to all other previous ligands, the electron-donating ligand ethyl 2-((4,7-dimethyl-1,4,7-triazonan-1-yl)methyl)isonicotinate (**Py$^{(OMe,Me)}$Me$_2$tacn**) was obtained following the scheme in **Figure 14**.

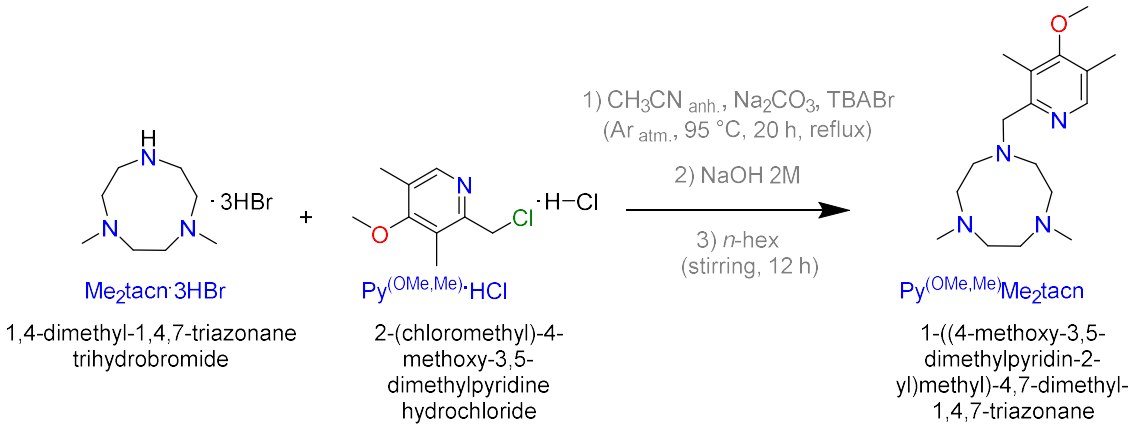

Figure 14. Synthetic scheme for the dimethylmethoxy ligand, 1-((4-methoxy-3,5-dimethylpyridin-2-yl)methyl)-4,7-dimethyl-1,4,7-triazonane (**Py$^{(OMe,Me)}$Me$_2$tacn**).

The distinctive feature of the ^{1}H-NMR spectrum of **Py$^{(OMe,Me)}$Me$_2$tacn** (**Figure 15**) is the absence of the β and β′ protons of the pyridine ring that were visible in all other spectra, and the signals corresponding to the -OC**H$_3$** protons at 3.78 ppm and two -C**H$_3$** signals at 2.40 ppm and 2.26 ppm with a 3 proton integral each.

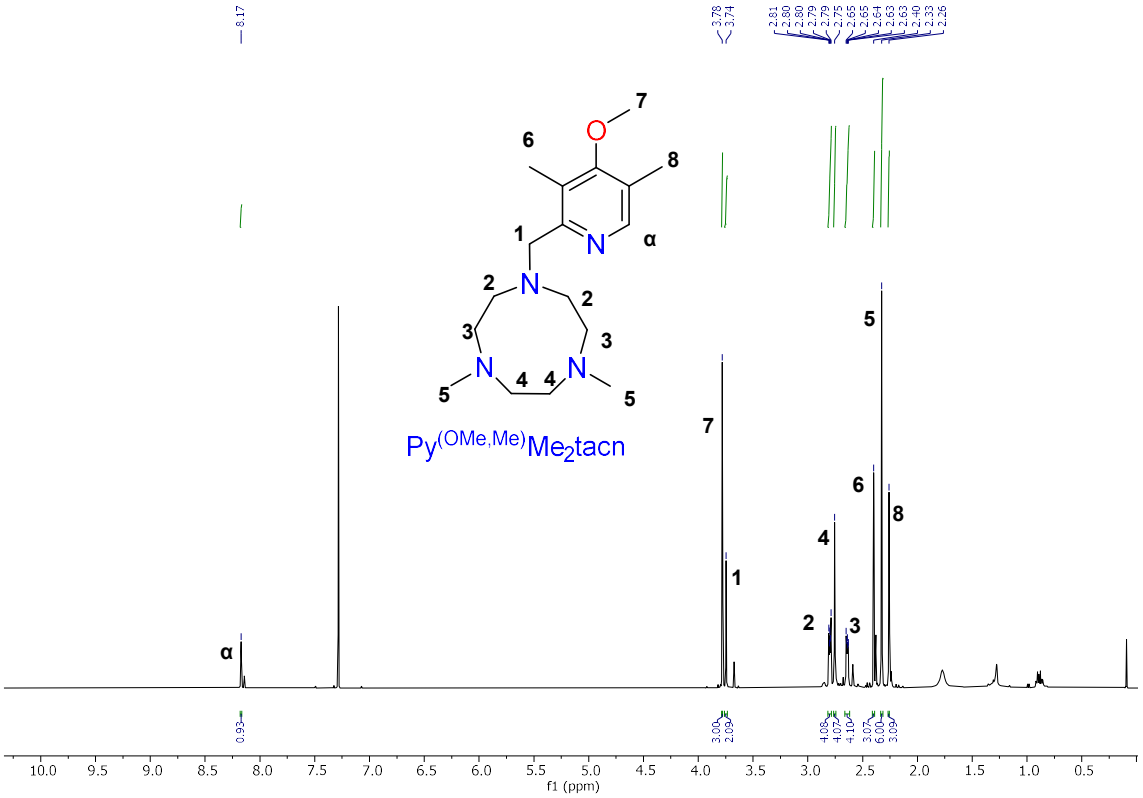

Figure 15. ^{1}H-NMR spectrum of 1-((4-methoxy-3,5-dimethylpyridin-2-yl)methyl)-4,7-dimethyl-1,4,7-triazonane (**Py$^{(OMe,Me)}$Me$_2$tacn**, $CDCl_3$, 500 MHz, 298 K).

To obtain the cobalt catalysts **Co(Py$^{(H,H)}$Me$_2$tacn)**, **Co(Py$^{(CN,H)}$Me$_2$tacn)**, **Co(Py$^{(COOEt,H)}$Me$_2$tacn)** and **Co(Py$^{(OMe,Me)}$Me$_2$tacn),** we reacted directly a stoichiometric amount of metal precursor and appropriate ligand dissolved in tetrahydrofuran (THF) by slowly adding the ligand to the metal salt solution. After overnight stirring and solvent removal, the residue was dissolved in CH_2Cl_2, filtered through Celite and crystalized by slow diffusion of Et_2O. The complexes were studied by paramagnetic ^{1}H-NMR spectroscopy in CD_3CN and showed the correct signals.

For **Co(Py$^{(H,H)}$Me$_2$tacn)**, the highest chemical shift at 224.52 ppm (**Figure 16**) corresponds to the α-hydrogen of the pyridine ring, being closest to the paramagnetic Co^{II} center. The β and β' pyridinic hydrogens (**Figure 16**, signals at 85.16 ppm and 61.11 ppm, respectively), while the remaining pyridinic γ-hydrogen is visible at 26.48 ppm (**Figure 16**). All signals were attributed based on available literature.[16]

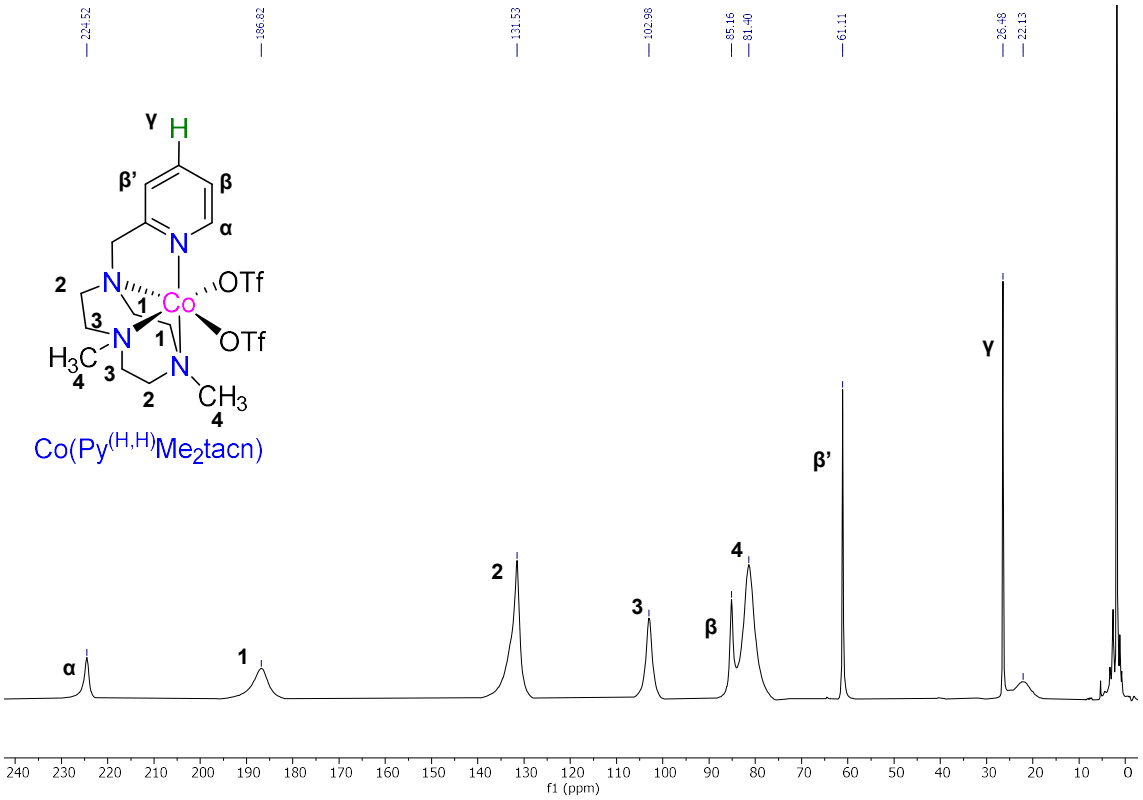

Figure 16. ^{1}H-NMR paramagnetic spectra of **Co(Py$^{(H,H)}$Me$_2$tacn)** (CD_3CN, 400 MHz, 298 K).

For **Co(Py$^{(CN,H)}$Me$_2$tacn)** the paramagnetic ^{1}H-NMR spectrum at room temperature in CD_3CN is shown in **Figure 17**. As literature explains, the chemical shift of the α-hydrogen (from 224.53 ppm in **Co(Py$^{(H,H)}$Me$_2$tacn)** to 212.70 ppm in **Co(Py$^{(CN,H)}$Me$_2$tacn)**) correlates with the electro-withdrawing properties of the cyan substituent in the pyridinic ring.[16]

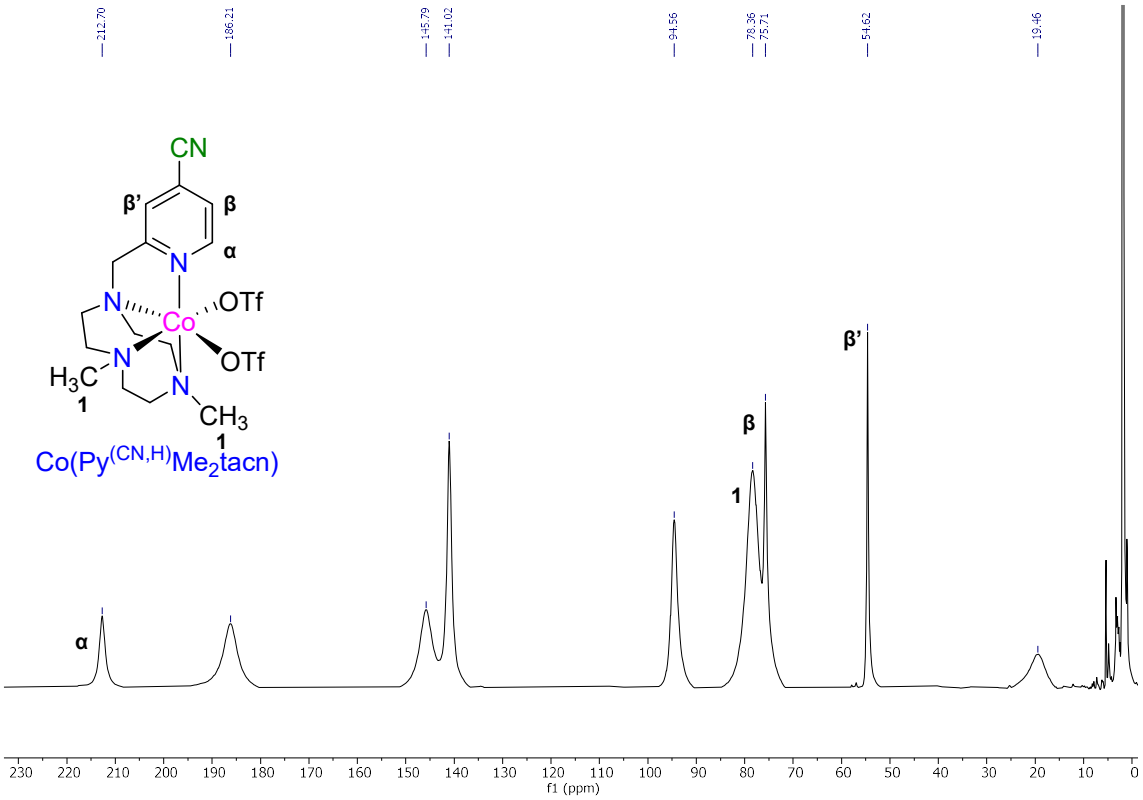

Figure 17. ^{1}H-NMR paramagnetic spectra of **Co(Py$^{(CN,H)}$Me$_2$tacn)** (CD_3CN, 400 MHz, 298 K).

The α-hydrogen in **Co(Py$^{(COOEt,H)}$Me$_2$tacn)** is shifted to 215.38 ppm **(Figure 18)**, an intermediate value between the two previous catalysts, as the electro-withdrawing effect of the -COOEt moiety is not as strong as in the case of the -CN group.

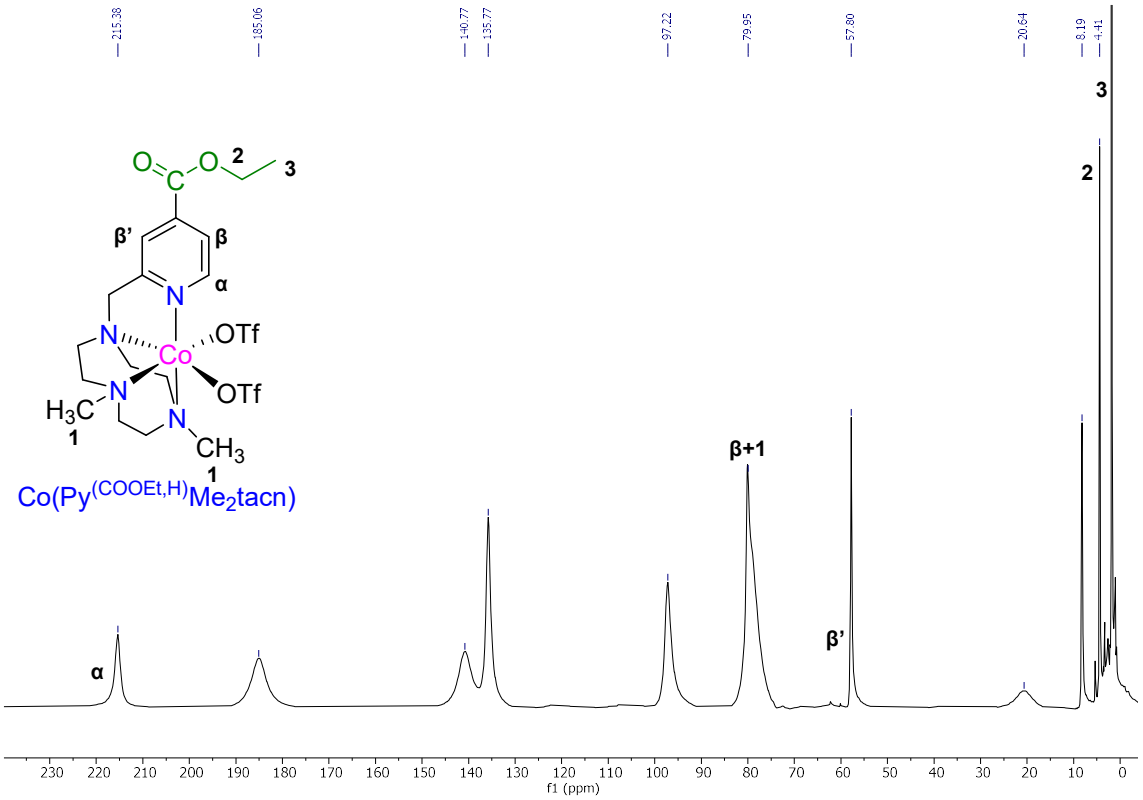

Figure 18. ^{1}H-NMR paramagnetic spectra of **Co(Py$^{(COOEt,H)}$Me$_2$tacn)** (CD_3CN, 400 MHz, 298 K).

For **Co(Py$^{(OMe,Me)}$Me$_2$tacn** the α-hydrogen is displaying the highest chemical shift of the series (**Figure 19**), the substituents in the pyridinic ring having the strongest electron-donating properties.

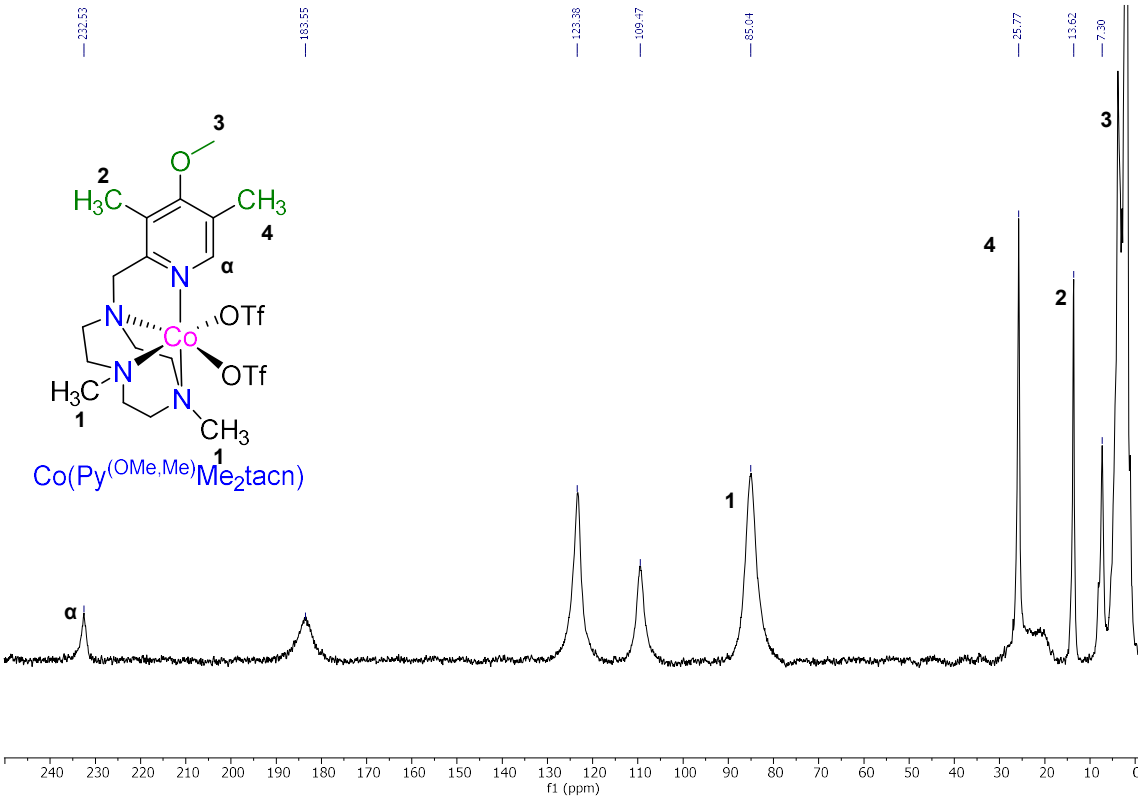

Figure 19. ^{1}H-NMR paramagnetic spectra of **Co(Py$^{(OMe,Me)}$Me$_2$tacn)** (CD_3CN, 400 MHz, 298 K).

3.2. Catalytic studies

3.2.1. Co(Py$^{(H,H)}$Me$_2$tacn)

The cyclic voltammogram (CV) performed under Ar atmosphere (**Figure 20**, black), of the hydrogen catalyst, **Co(Py$^{(H,H)}$Me$_2$tacn),** shows 2 irreversible cathodic peaks (**Figure 20**, left), the first peak, at -1.751 V, being isolated in **Figure 20**, right, and corresponding to a $Co^{II/I}$ process. The second peak, at -2.36 V, corresponds to a formal $Co^{I/0}$ process (where the e^- is delocalized in the pyridine ring). Under CO_2 atmosphere the first peak suffers an anodic shift of 40 mV (**Figure 20**, right, red). On the back scan, a corresponding oxidation peak is noticed at -0.71 V and this change in the redox peak indicates the strong reaction between $Co^{(I)}$ and CO_2 with the formation of a new species. The second cathodic peak under CO_2 is marked by a 4.2 times current increase (**Figure 20**, left, red) corresponding to the electrocatalytic reduction of CO_2 by the formal Co^0 species.

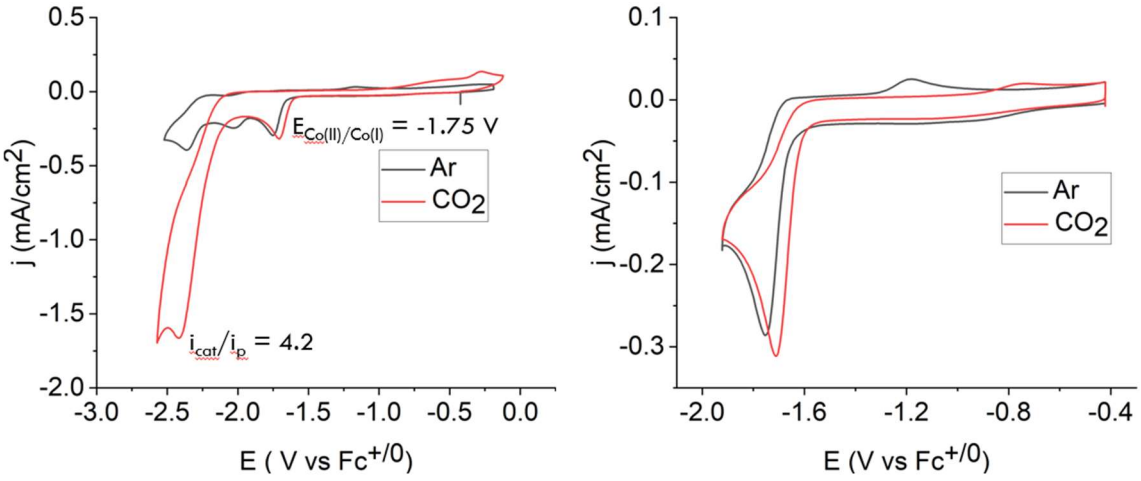

Figure 20. Cyclic voltammogram of **Co(Py$^{(H,H)}$Me$_2$tacn)** (1 mM) in TBAPF$_6$/CH$_3$CN (0.1 M) under argon (black) and carbon dioxide (red) atmosphere.

The effect of the proton source was studied by titrations with increased amounts of MeOH (**Figure 21**, right). Easily observable at MeOH concentration of 3.53 M is the 15.2 times current increase in the second cathodic peak (**Figure 21**, left, green), proving that the mechanism is influenced by the proton source concentration. This current increase is not visible in the first reduction wave at -1.75 (**Figure 21**, red), showing that the reaction of Co^{I} species is not affected by the proton concentration. A maximum effect was observed at MeOH concentration of 3.53 M (**Figure 21**, right) and this value was used in all subsequent CPE experiments, in dark as well as under light irradiation.

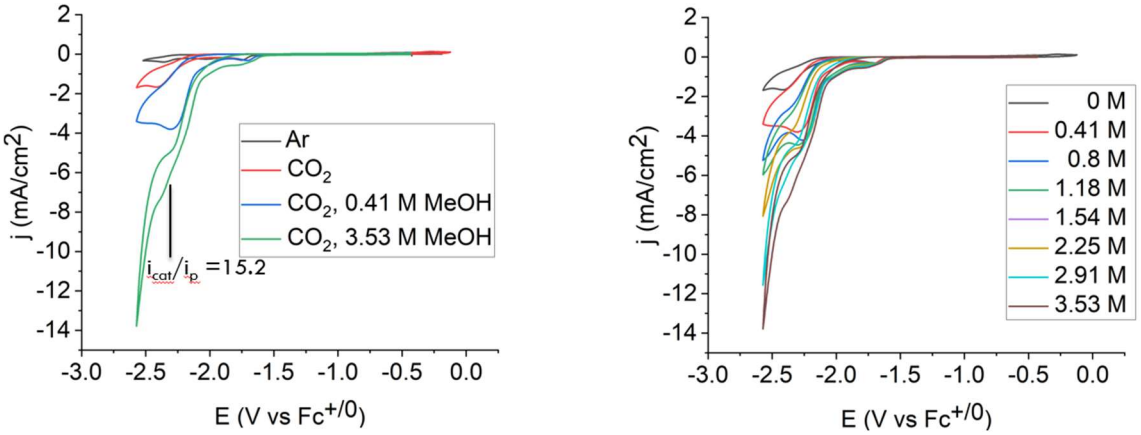

Figure 21. CVs of **Co(Py$^{(H,H)}$Me$_2$tacn)** (1 mM) in TBAPF$_6$/CH$_3$CN (0.1 M) with different amounts of MeOH, under Ar and CO_2 atmosphere.

Controlled-potential electrolysis (CPE) experiments in the dark at an applied potential of -2.39 V with MeOH 3.53 M, resulted in a Faraday efficiency (FE_{CO}) of 19% and turnover number (TON_{CO}/2 h) of 1.9.

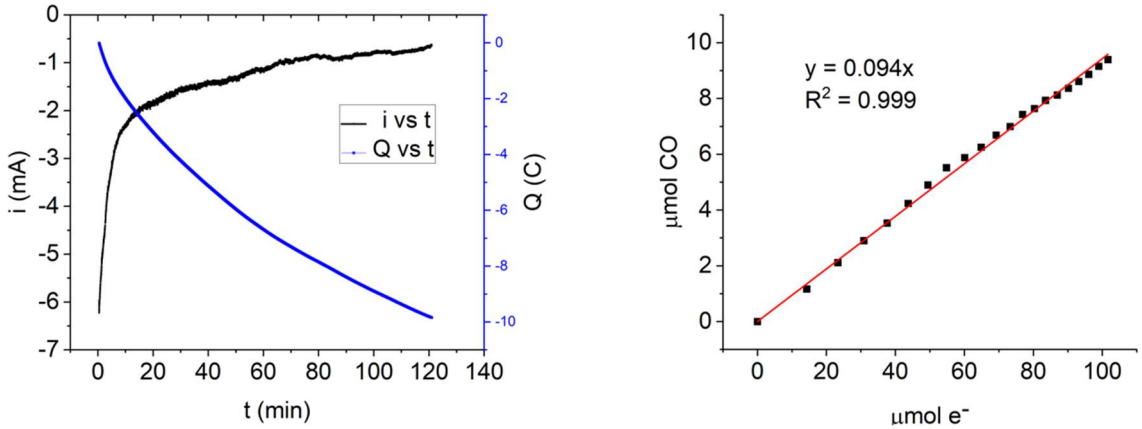

Figure 22. CPE in the dark of **Co(Py$^{(H,H)}$Me$_2$tacn)** (0.86 mM) in TBAPF$_6$/CH$_3$CN (86 mM) with MeOH (3.53 M), constant CO_2 flow. Current (i, left, black) and charge (Q, left, blue) passed over 120 minutes at E = -2.39 V.

When the CPE was repeated under light irradiation at -2.38 V applied potential, the FE_{CO} increased almost two-fold to 35% and TON_{CO}/2 h increased almost 3 times, to 5.9.

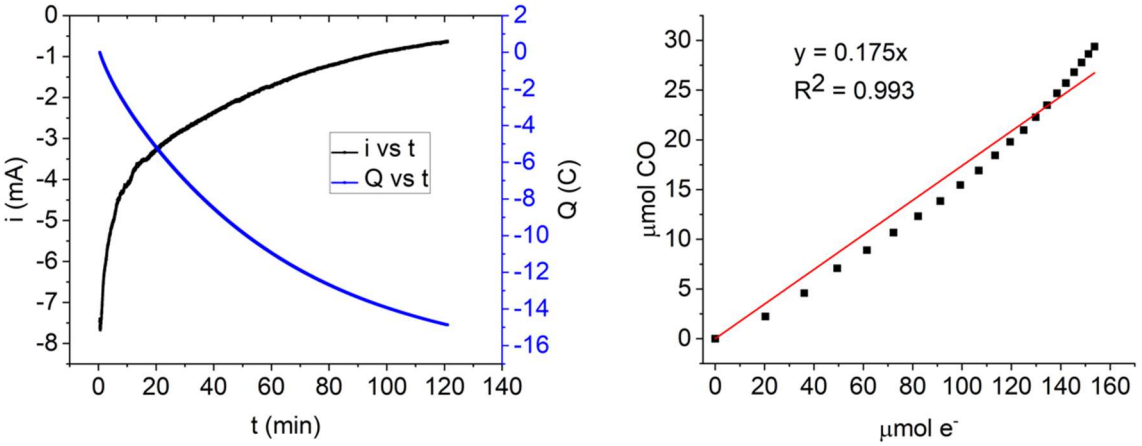

Figure 23. Light-assisted (447 nm) CPE of **Co(Py$^{(H,H)}$Me$_2$tacn)** (0.86 mM) in TBAPF$_6$/CH$_3$CN (86 mM) with MeOH (3.53 M), constant CO_2 flow, over 120 minutes at E = -2.38 V.

A comparison of CV and CPE performed under dark *vs.* light irradiation for **Co(Py$^{(H,H)}$Me$_2$tacn)** can be seen in **Figure 24**. The current increase in the light-assisted measurements (red *vs.* black) results in higher TON and FE numbers.

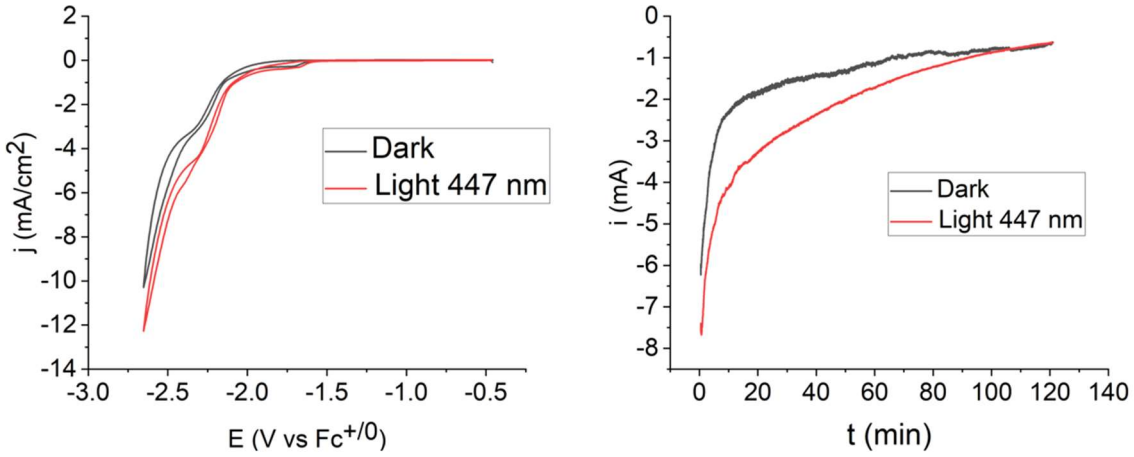

Figure 24. Co(Py$^{(H,H)}$Me$_2$tacn) in $TBAPF_6/CH_3CN$ (86 mM) with MeOH (3.53 M), constant CO_2 flow. Left: CV comparison performed in dark (black) and under light irradiation (red). Right: CPE comparison performed in dark (black) and under light irradiation (red).

3.2.2. Co(Py$^{(CN,H)}$Me$_2$tacn)

The CV under argon of the catalyst with cyan substituent (**Figure 25**, left) presented a first cathodic peak at -1.47 V (a more positive potential than the hydrogen analogue) corresponding to the $Co^{II/I}$ transition. Unlike the hydrogen catalyst, no anodic shift was observed this time in the presence of CO_2 at the first reduction wave. In CO_2 atmosphere, without a proton source (**Figure 25**, right, black) the second reductive wave that should correspond to the catalytic electroreduction of CO_2 is barely visible, while with the addition of MeOH (red and blue) the catalytic wave is observed at a more positive potential and with significant current increase, signaling increased catalytic activity i_{cat}/i_p = 7.2 of the cobalt complex.

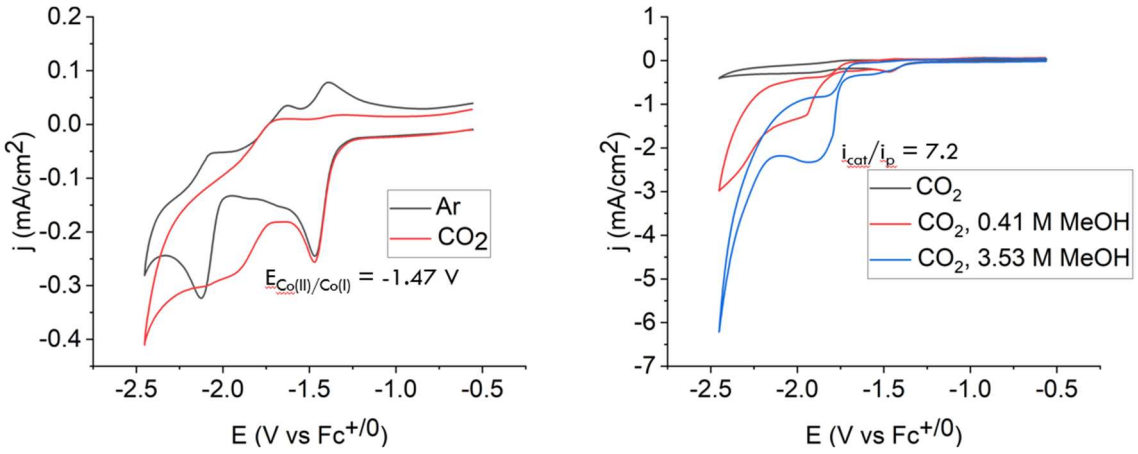

Figure 25. CV of **Co(Py$^{(CN,H)}$Me$_2$tacn)** (1 mM) in TBAPF$_6$/CH$_3$CN (0.1 M) under argon and carbon dioxide. Left: without MeOH. Right: with different concentrations of MeOH (0.41 M in red and 3.53 M in blue).

CPE of **Co(Py$^{(CN,H)}$Me$_2$tacn)** under dark **(Figure 26)** at an applied potential of -1.98 V resulted in FE$_{CO}$ of 51% and TON$_{CO}$/1.5 h of 3.6.

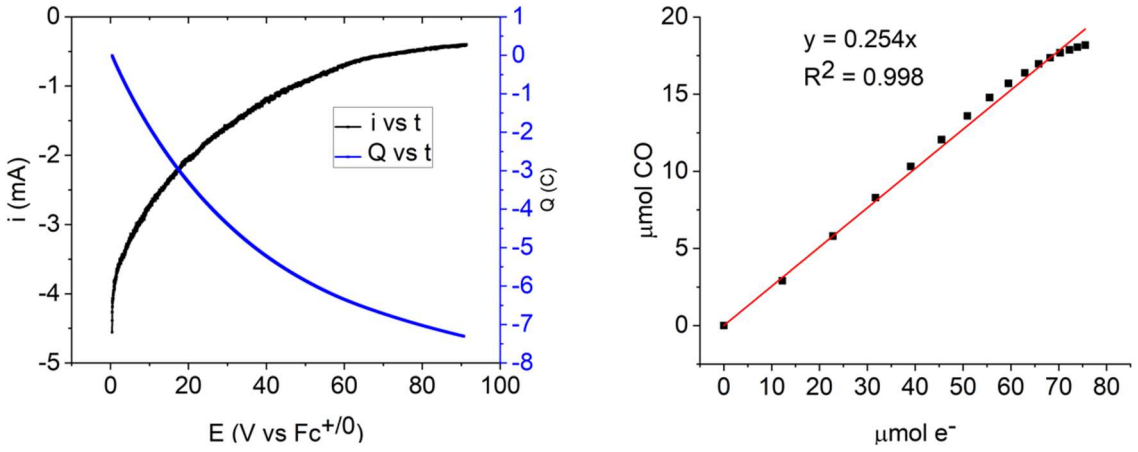

Figure 26. CPE in the dark of **Co(Py$^{(CN,H)}$Me$_2$tacn)** (0.86 mM) in TBAPF$_6$/CH$_3$CN (86 mM) with MeOH (3.53 M), constant CO$_2$ flow, over a 90 minutes time period at E = -1.98 V.

Light-assisted CPE of **Co(Py$^{(CN,H)}$Me$_2$tacn) (Figure 27)** performed for 90 minutes at a potential of -1.97 V, resulted in FE$_{CO}$ of 52% and TON$_{CO}$/1.5 h of 4.3.

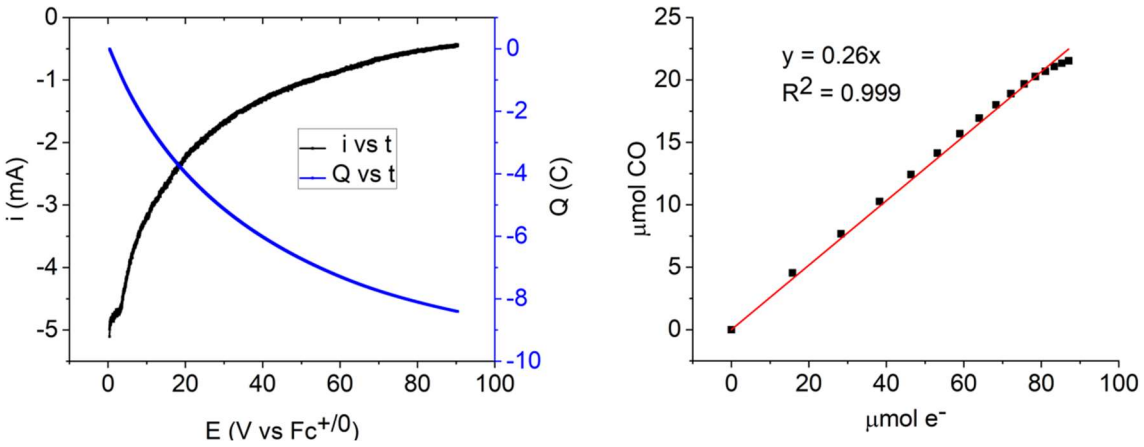

Figure 27. Light-assisted (447 nm) CPE of **Co(Py$^{(CN,H)}$Me$_2$tacn)** (0.86 mM) in TBAPF$_6$/CH$_3$CN (86 mM) with MeOH (3.53 M), constant CO_2 flow, over 90 minutes at E = -1.97 V.

A comparison of CV and CPE performed under dark *vs.* light-assisted for **Co(Py$^{(CN,H)}$Me$_2$tacn)** can be seen in **Figure 28**. Little to no effect of the light irradiation can be seen in terms of FE_{CO} and only a 20% increase in TON_{CO} compared to the results in dark.

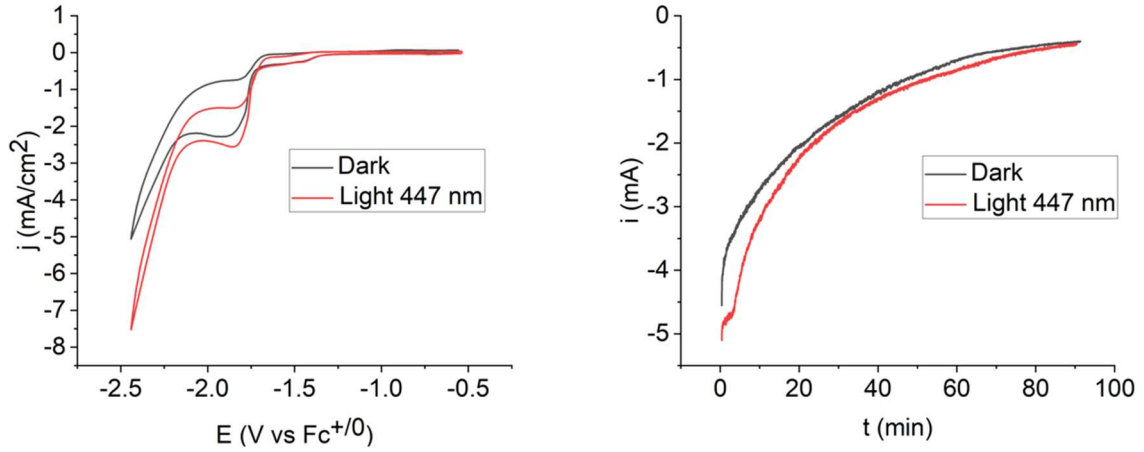

Figure 28. Co(Py$^{(CN,H)}$Me$_2$tacn) in TBAPF$_6$/CH$_3$CN (86 mM) with MeOH (3.53 M), constant CO_2 flow. Left: CV comparison performed in dark (black) and under light irradiation (red). Right: CPE comparison performed in dark (black) and under light irradiation (red).

3.2.3. Co(Py$^{(COOEt,H)}$Me$_2$tacn)

The CV of the ester catalyst (**Figure 29,** left) was similar to the cyan catalyst and presented a first reduction peak at -1.57 V corresponding to the $Co^{II/I}$ transition. The second peak that is corresponding to the electroreduction of CO_2 is almost absent (**Figure 29,** right, black) without the addition of MeOH but clearly visible with MeOH, accompanied by a 8.9 times increase in current at MeOH concentration of 3.53 M. The electronic-withdrawing effect of the ester group is less pronounced compared to the cyan group, but still very distinct compared to the hydrogen catalyst.

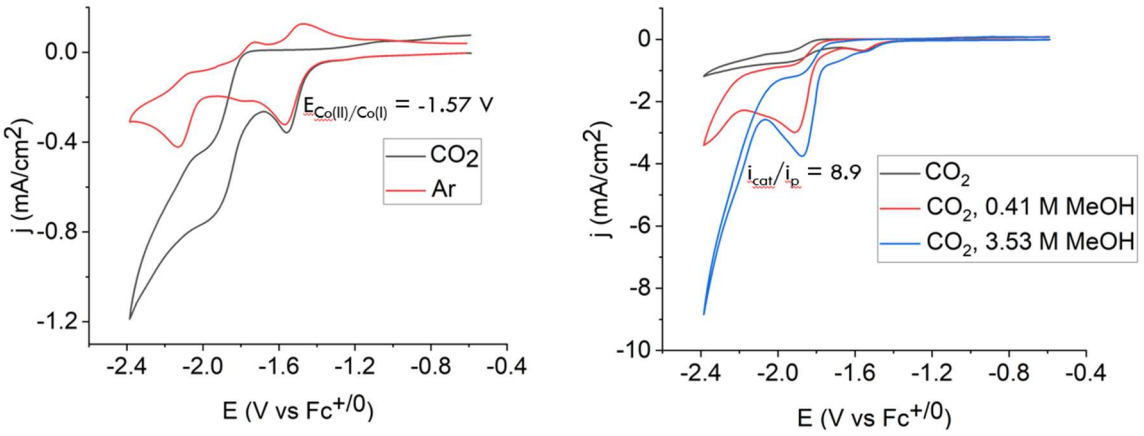

Figure 29. CV of **Co(Py$^{(COOEt,H)}$Me$_2$tacn)** (1 mM) in $TBAPF_6/CH_3CN$ (0.1 M) under argon (red) and carbon dioxide (black). Left: without MeOH. Right: with different concentrations of MeOH (0.41 M in red and 3.53 M in blue).

CPE of **Co(Py$^{(COOEt,H)}$Me$_2$tacn)** under dark **(Figure 30)** at an applied potential of -1.98 V resulted in FE_{CO} of 39% and TON_{CO}/2 h of 6, performing similarly but slightly worse in terms of FE_{CO} and TON_{CO} compared to **Co(Py$^{(CN,H)}$Me$_2$tacn).**

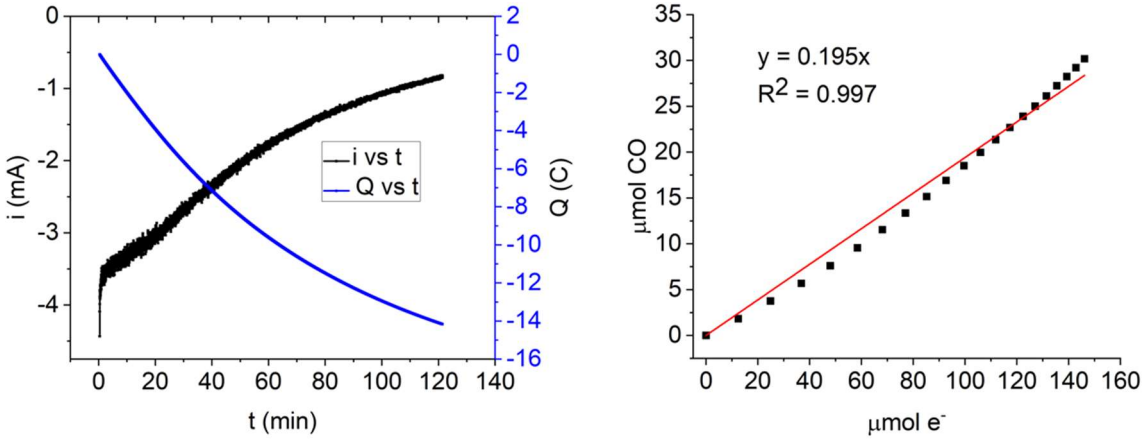

Figure 30. CPE in the dark of **Co(Py$^{(COOEt,H)}$Me$_2$tacn)** (0.86 mM) in TBAPF$_6$/CH$_3$CN (86 mM) with MeOH (3.53 M), constant CO_2 flow, over a 120 minutes time period at E = -1.98 V.

Light-assisted CPE of **Co(Py$^{(COOEt,H)}$Me$_2$tacn) (Figure 31)** performed for 120 minutes at a potential of -1.99 V, and resulted in FE_{CO} of 44% and TON_{CO}/2 h of 8.8, showing slight increase in FE and a more significant 46% increase in TON with light irradiation over dark.

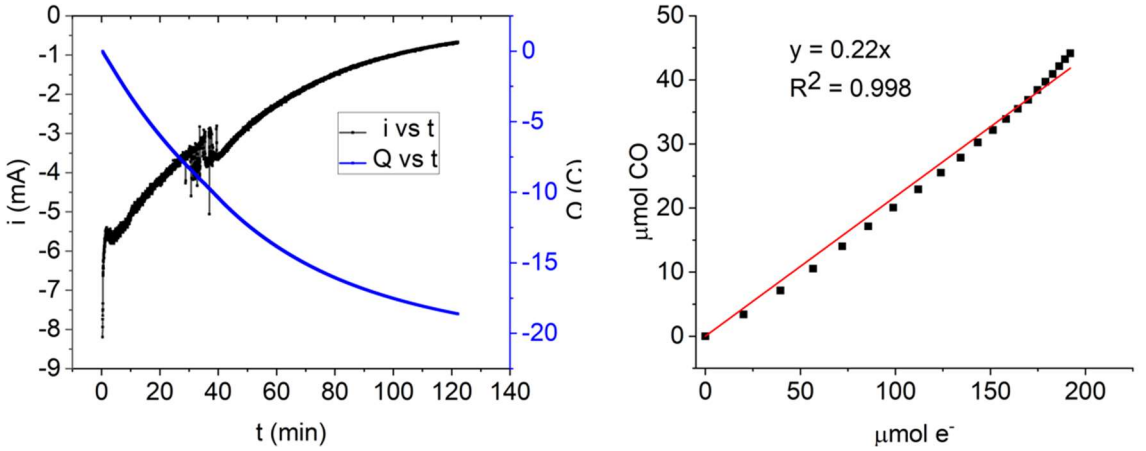

Figure 31. Light-assisted (447 nm) CPE of **Co(Py$^{(COOEt,H)}$Me$_2$tacn)** (0.86 mM) in TBAPF$_6$/CH$_3$CN (86 mM) with MeOH (3.53 M), constant CO_2 flow, over 120 minutes at E = -1.99 V.

A comparison of CV and CPE performed under dark *vs.* light-assisted for **Co(Py$^{(COOEt,H)}$Me$_2$tacn)** can be seen in **Figure 32**. The contribution of light irradiation to

catalytic activity is minimal, resulting in similar FE but higher TON compared to the cyan catalyst.

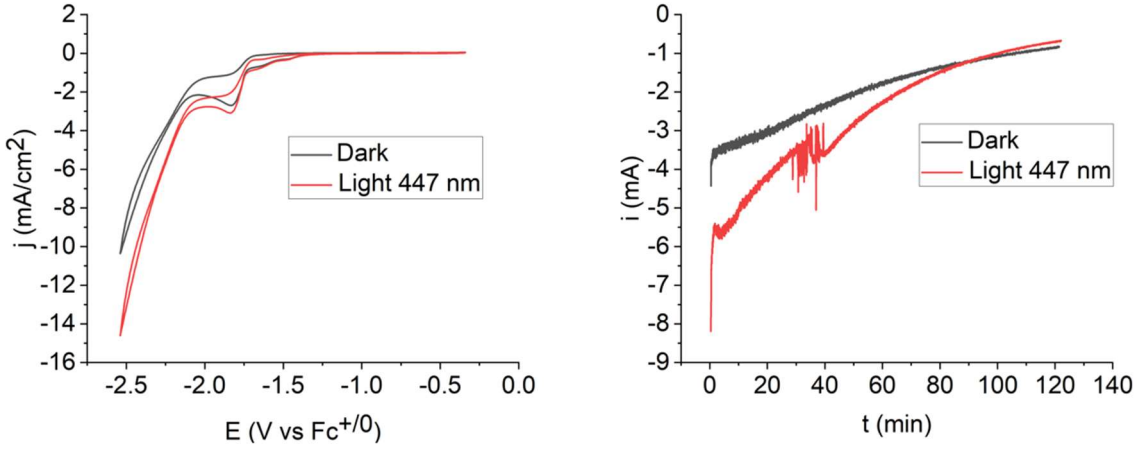

Figure 32. Co(Py$^{(COOEt,H)}$Me$_2$tacn) in $TBAPF_6/CH_3CN$ (86 mM) with MeOH (3.53 M), constant CO_2 flow. Left: CV comparison performed in dark (black) and under light irradiation (red). Right: CPE comparison performed in dark (black) and under light irradiation (red).

3.2.4. Co(Py$^{(OMe,Me)}$Me$_2$tacn)

The CV of the dimethyl methoxy catalyst (**Figure 33**) behaved similar to the hydrogen catalyst showing an anodic shift in the presence of CO_2. The first reduction peak corresponding (**Figure 33**, right) to the $Co^{II/I}$ transition was recorded at -1.79 V, slightly more negative than the hydrogen catalyst, due to the stronger electron-donating effect of the -Me and -OMe substituents in **Co(Py$^{(OMe,Me)}$Me$_2$tacn).** The increase in current (i_{cat}/i_p = 3.7) that is observed under CO_2 compared to under Ar shows the existence of catalytic activity. However, in **Figure 34** it can be observed that the presence of MeOH has a big impact on the increase of current under CO_2 flow, showing the importance of protons in the catalytic process for **Co(Py$^{(OMe,Me)}$Me$_2$tacn).**

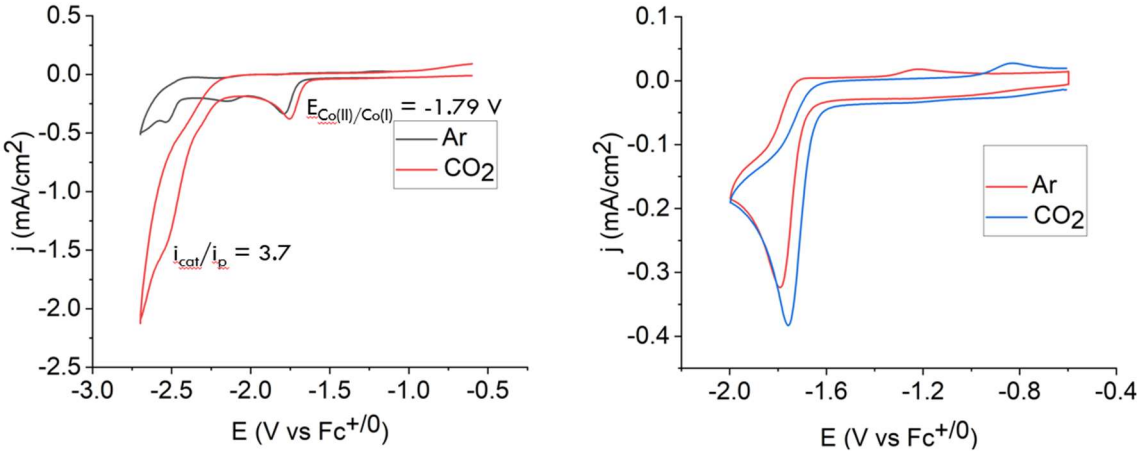

Figure 33. CV of **Co(Py$^{(OMe,Me)}$Me$_2$tacn)** (1 mM) in TBAPF$_6$/CH$_3$CN (0.1 M) under Ar and CO_2 atmosphere.

Interestingly, for **Co(Py$^{(OMe,Me)}$Me$_2$tacn)** an anodic shift increase for the first reduction wave is observed with increase in the concentration of the proton source signaling that the process taking place at the first wave is influenced by the proton source, unlike with the other 3 studied catalysts.

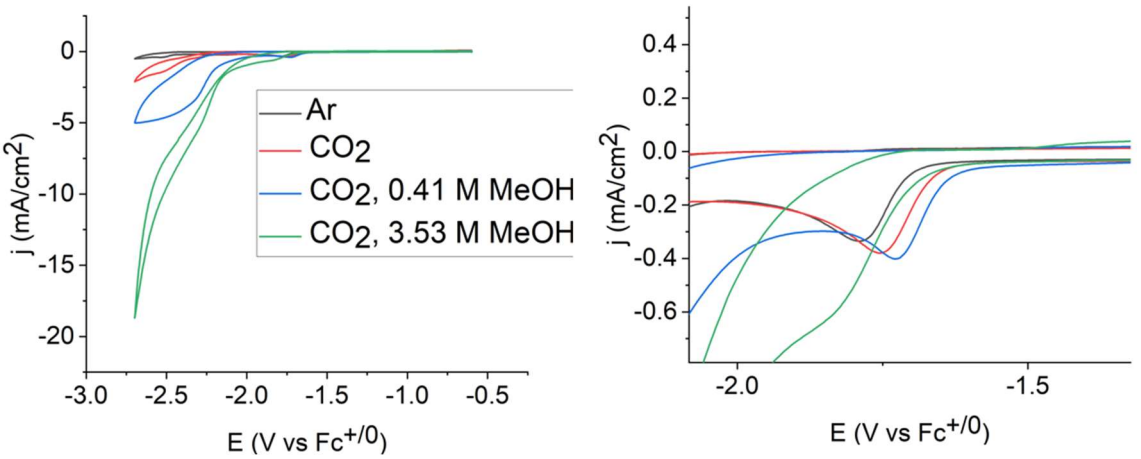

Figure 34. CV of **Co(Py$^{(OMe,Me)}$Me$_2$tacn)** (1 mM) in TBAPF$_6$/CH$_3$CN (0.1 M) under Ar and CO_2 atmosphere without and with different concentrations of MeOH.

CPE of **Co(Py$^{(OMe,Me)}$Me$_2$tacn)** under dark **(Figure 35)** at an applied potential of -2.39 V resulted in a very low FE_{CO} of 6% and TON_{CO}/2 h of 2.1. In these conditions hydrogen evolution was also recorded with FE_{H_2} of 55% and TON_{H_2} of 26, one order of magnitude higher than for CO.

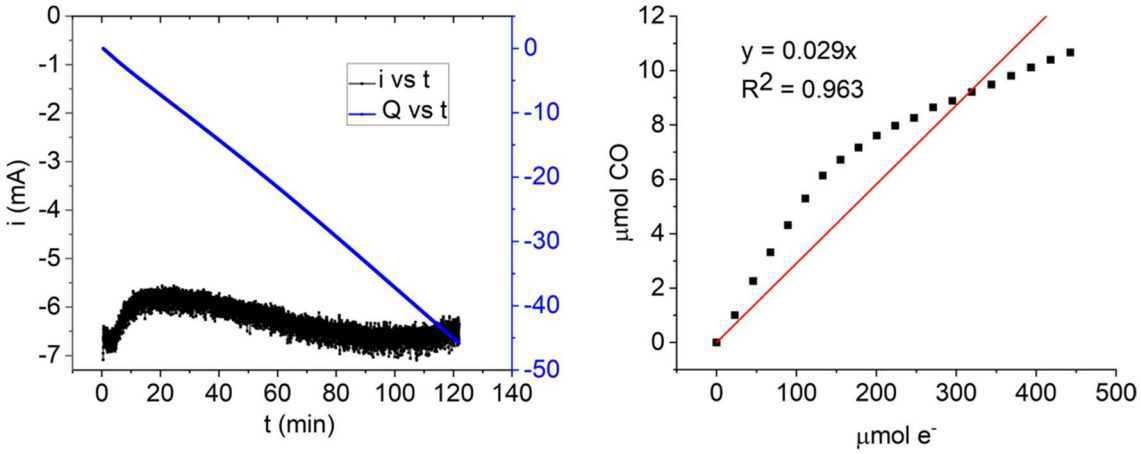

Figure 35. CPE in the dark of **Co(Py$^{(OMe,Me)}$Me$_2$tacn)** (0.86 mM) in TBAPF$_6$/CH$_3$CN (86 mM) with MeOH (3.53 M), constant CO_2 flow, over a 120 minutes time period at E = -2.39 V.

Light-assisted CPE of **Co(Py$^{(OMe,Me)}$Me$_2$tacn) (Figure 36)** performed for 120 minutes at a potential of -2.40 V, had a FE_{CO} of 14% and TON_{CO}/2 h of 5.8, showing a higher increase ratio (but lower FE) with light irradiation as the hydrogen catalyst, **Co(Py$^{(H,H)}$Me$_2$tacn).**

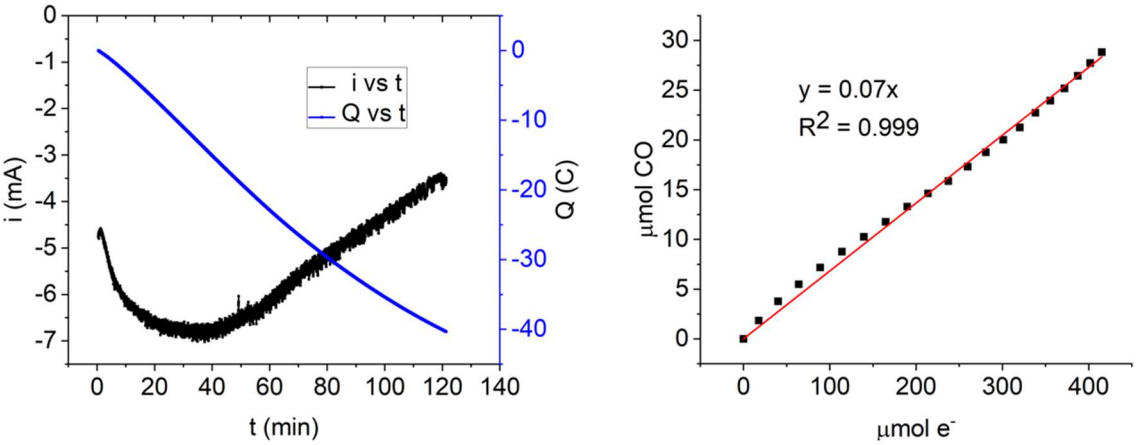

Figure 36. Light-assisted (447 nm) CPE of **Co(Py$^{(OMe,Me)}$Me$_2$tacn)** (0.86 mM) in TBAPF$_6$/CH$_3$CN (86 mM) with MeOH (3.53 M), constant CO_2 flow, over 120 minutes at E = -2.40 V.

Comparing dark *vs*. light conditions for CV and CPE for **Co(Py$^{(OMe,Me)}$Me$_2$tacn)** can be seen in **Figure 37**. The hydrogen evolution process taking place at a more positive potential is competing with the CO_2 reduction catalysis that happens at a more negative

potential. However, light irradiation did help increase the FE and TON in the case of CO formation but is not affecting FE and TON for hydrogen evolution.

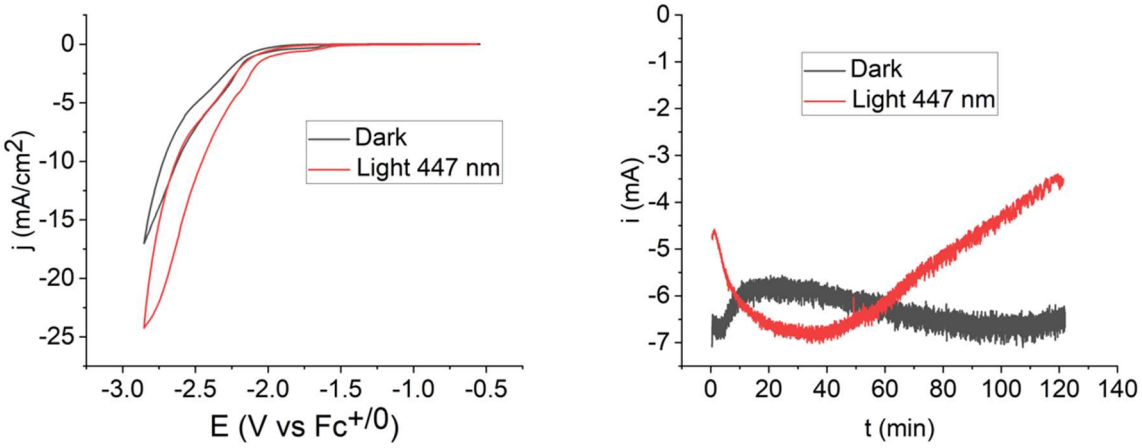

Figure 37. Co(Py$^{(OMe,Me)}$Me$_2$tacn) in $TBAPF_6/CH_3CN$ (86 mM) with MeOH (3.53 M), constant CO_2 flow. Left: CV comparison performed in dark (black) and under light irradiation (red). Right: CPE comparison performed in dark (black) and under light irradiation (red).

To summarize, the CPE results for the four studied catalysts are presented in **Table 1**.

Table 1. Comparison of CPE catalysis results for studied cobalt complexes, under light irradiation and under dark.

Catalyst	FE_{CO} dark	FE_{CO} light	TON_{CO} dark	TON_{CO} light	TON increase (times)
Co(Py$^{(H,H)}$Me$_2$tacn)	19 %	35 %	1.9 (2 h)	5.9 (2 h)	× 3.1
Co(Py$^{(CN,H)}$Me$_2$tacn)	51 %	52 %	3.6 (1.5 h)	4.3 (1.5 h)	× 1.2
Co(Py$^{(COOEt,H)}$Me$_2$tacn)	39 %	44 %	6.0 (2 h)	8.8 (2 h)	× 1.5
Co(Py$^{(OMe,Me)}$Me$_2$tacn)	6 %	14 %	2.1 (2 h)	5.8 (2 h)	× 2.8

4. Experimental section

4.1. Instrumentation

^{1}H-NMR. Bruker AV400 and AV500 spectrometers were used to record all nuclear magnetic resonance (NMR) spectra, under normal conditions (298 K), and every ^{1}H chemical shift was expressed in parts per million.

Electrochemistry. A VSP potentiostat from Bio-Logic was used together with the EC-Lab software for recording the results. The experiments were carried out in a one-compartment, double-walled glass cell fitted with glassy carbon (GC) working electrodes, Pt wire (inside a glass chamber with fritted tip filled with the same electrolyte solution as the cell) as counter electrode and Ag/AgCl wire immersed in a glass tube with fritted tip (same electrolyte solution) as pseudo-reference electrode. Working electrodes were cleaned with alumina powder (0.05 µm, CHInstruments) on a polishing pad with distilled H_2O, then washed with distilled H_2O and acetone, and finally by sonication. Ar/CO_2 gas flow was controlled with mass-flow controllers from Alicat.

Cyclic voltammetry (CV) measurements were done in inert gas atmosphere (Ar) or CO_2 with 3 mL solutions of Co complexes (1 mM) in degassed CH_3CN, with tetrabutylammonium hexafluorophosphate ($TBAPF_6$) 0.1 M as supporting electrolyte. The working electrode used was GC (0.3 cm ø). As an internal standard, Ferrocene (Fc) was added. All potentials are referenced *vs*. the $Fc^{+/0}$ redox couple. Scan rate for all CVs was 100 mV/s. Presented $E_{1/2}$ values are the average of the oxidative and reductive peak potentials $(E_{pa}+E_{pc})/2$.

Controlled-potential electrolysis (CPE) was performed in the same CPE setup described above, under constant CO_2 gas flow, with constant stirring and controlled temperature (25 ˚C). 5 mL of the same electrolyte as in the CV experiment were used ($TBAPF_6/CH_3CN_{anh.}$, 0.086 M). The working electrode was GC. As **proton source**, 0.8 mL of MeOH were added to the electrolyte 15 minutes before starting the measurements. The catalyst concentration in the final volume was 0.86 mM. The **light-assisted CPEs** were performed using irradiation provided by a 16 LED blue lamp (Toshiba 45 W Luxeon Rebel, 447 ± 2.5 nm).

Gas chromatography. Agilent 490 micro gas chromatograph with thermal conductivity detector and a Molesieve 5 Å column was used to analyze the gas resulting from

electrochemistry experiments. The gas output of each CPE was analyzed via on-line gas chromatography every 5 minutes during the experiments. The measurement and quantification of obtained carbon monoxide and hydrogen was calculated through the interpolation of previously performed calibrations.

4.2. Materials

Chemicals were used as purchased from manufacturers without any further purification steps. 1,4,7-tritosyl-1,4,7-triazonane was obtained from WeylChem Catexel, HBr 33% in AcOH from Acros Organics, HBr 48% from Carlo Erba Reagents. Tetrabutylammonium hexafluorophosphate ($TBAPF_6$, Sigma-Aldrich, ≥ 99.0%) was dried in the oven for 24 h, placed under vacuum and kept in argon atmosphere. All other reagents were sourced from Sigma-Aldrich. Water was purified with a Milli-Q Millipore Gradient AIS system.

4.3. Synthesis of ligands

All ligands were synthesized in a similar fashion, following the scheme from **Figure 38**:

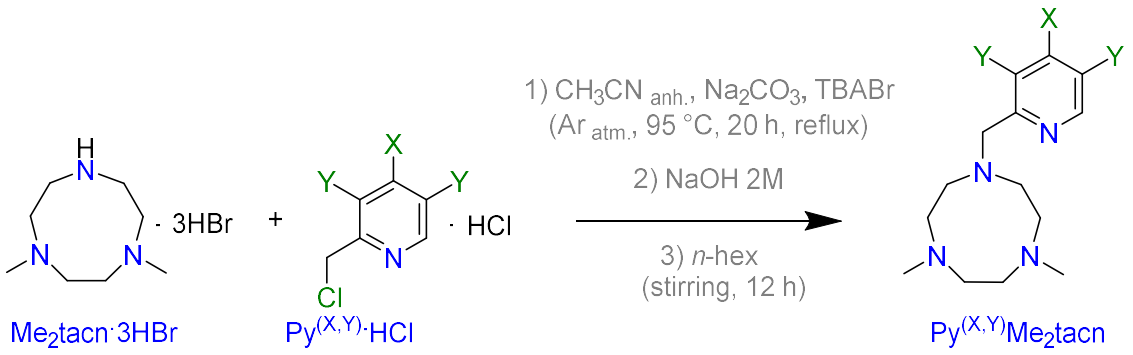

Figure 38. General synthesis procedure of ligands starting from 1,4-dimethyl-1,4,7-triazonane trihydrobromide (**Me_2tacn·3HBr**) and a differently substituted 2-chloromethyl pyridine ($Py^{(X,Y)}$·HCl).

The triazonane substrate (**Me_2tacn·3HBr**) was synthesized starting from 1,4,7-tritosyl-1,4,7-triazonane (WeylChem Catexel).

Pyridine substrates with hydrogen ($Py^{(H,H)}$·HCl) and dimethyl methoxy ($Py^{(OMe,Me)}$·HCl) were obtained commercially and used as such without any further purifications. **$Py^{(CN,H)}$·HCl** was synthesized from commercially available isonicotinonitrile. **$Py^{(COOEt,H)}$·HCl** was synthesized starting from commercially available pyridine-2,4-dicarboxylic acid.

4.3.1. Synthesis of triaza substrate: 1,4-dimethyl-1,4,7-triazonane (Me_2tacn·3HBr).

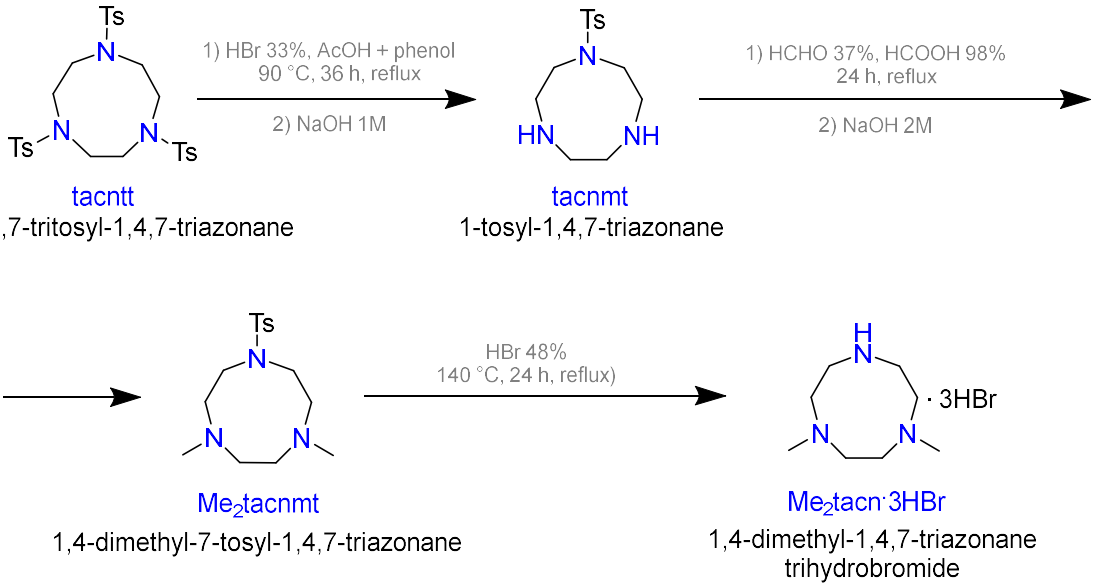

Figure 39. Synthesis procedure of 1,4-dimethyl-1,4,7-triazonane trihydrobromide (**Me_2tacn·3HBr**) starting from 1,4,7-tritosyl-1,4,7-triazonane (tacnmt).

1-tosyl-1,4,7-triazonane (tacnmt). In a 1000 mL two-neck round-bottom flask fitted for reflux with gas traps and drip funnel, 1,4,7-tritosyl-1,4,7-triazonane (24.6 g, 41.6 mmol) were mixed with phenol (35.2 g, 374 mmol). Then, HBr 33% in CH_3COOH (380 mL), was added dropwise. The mixture was heated at 90 °C for 36 h, with continuous stirring. The solids dissolved slowly and a high release of HBr gas was observed. After a few hours, a white precipitate appeared in the solution (which started out yellow and became brown later). At the end of 36 hours, the liquid was dark brown with a significant amount of white precipitate present. The mixture allowed to reach room temperature. The precipitate was filtered under vacuum, washed and sonicated in diethyl ether (Et_2O) to remove as much of the impurities as possible then filtered again. At this point the compound was an off-white precipitate. To the precipitate was added NaOH (320 mL,

1M) and the resulting salmon-pink mixture extracted with CH_2Cl_2 (3 times with 190 mL). The organic phase was dried on anhydrous $MgSO_4$. After filtration, the solvent was evaporated in the rotary evaporator to obtain a cream opaque oil that was dried under vacuum overnight to get 7.26 g of white solid **tacnmt** (25.6 mmol, 61.5% yield). ^{1}H-NMR ($CDCl_3$, 500 MHz, 298 K) δ, ppm: 7.69 (d, J = 10 Hz, 2H, Ar**H**), 7.33 (d, J = 10 Hz, 2H, Ar**H**), 3.26 (m, 4H, TsN-C**H$_2$**-CH$_2$-NH), 3.15 (m, 4H, TsN-CH$_2$-C**H$_2$**-NH), 3.00 (s, 4H, HN-C**H$_2$**-C**H$_2$**-NH), 2.44 (s, 3H, Ar-C**H$_3$**).

1,4-dimethyl-7-tosyl-1,4,7-triazonane (Me$_2$tacnmt). tacnmt (7.26 g, 25.6 mmol) were solubilized in formaldehyde 37% (20.5 mL) and formic acid 98% (20.5 mL). A yellow color developed and the solution was refluxed for 24 h. Once at room temperature, HCl 36.5% (8.5 mL) were added to the mixture and stirred for another 10 min. After removing the solvent (rotary evaporator), water (9.5 mL) was added to the viscous yellow residue and the pH of the mixture was adjusted to 14 by the addition of NaOH 2M in great excess (approximately 300 mL). The mixture was stirred for 20 h at room temperature during which time a white precipitate formed. The precipitate was filtered and dissolved in CH_2Cl_2 (50 mL). NaOH (50 mL, 5M) was added and an extraction with CH_2Cl_2 (3 times 50 mL) was performed. The organic filtrate was dried on $MgSO_4$ and the solvent was evaporated and **Me$_2$tacnmt** was recovered as white solid (6.55 g, 21 mmol, 82% yield). ^{1}H-NMR ($CDCl_3$, 500 MHz, 298 K) δ, ppm: 7.69 (d, J = 10 Hz, 2H, Ar**H**), 7.32 (d, J = 10 Hz, 2H, Ar**H**), 3.27 (m, 4H, TsN-C**H$_2$**-CH$_2$-NH), 3.15 (m, 4H, TsN-CH$_2$-C**H$_2$**-NH), 3.00 (s, 4H, HN-C**H$_2$**-C**H$_2$**-NH), 2.44 (s, 3H, Ar-C**H$_3$**). The NH signal (2H) around 1.85 ppm is not visible on the spectra likely due to H_2O traces in the NMR sample.

1,4-dimethyl-1,4,7-triazonane trihydrobromide (Me$_2$tacn·3HBr). Me$_2$tacnmt (6.55 g, 21 mmol) was dissolved in HBr 48% (67 mL) added dropwise, and refluxed at 140 °C for 24 h, with stirring. Once cooled to room temperature, the black residue was placed in the rotary evaporator and dried (approximately 3 h). Once dry, acetone (100 mL) was added and left under stirring overnight. A white precipitate developed in a brown solution, which was then separated via vacuum filtration (quickly due to the compound's hygroscopicity), then sonicated in acetone for 5 minutes, filtered again and finally dried to remove all acetone in the rotary evaporator. Once completely dry, it was dissolved in water (100 mL). Using NaOH 2M, the solution was brought to pH 5 and an extraction

using CH_2Cl_2 (3 times 100 mL) was performed. Continuing to add NaOH, pH 7 was achieved and another extraction with CH_2Cl_2 (3 times 100 mL) was done. Finally, the pH was adjusted to 14 and one extraction with CH_2Cl_2 (100 mL) was performed. The filtrate was dried on anhydrous $MgSO_4$ and then in the rotary evaporator. After that, another CH_2Cl_2 extraction (2 times 100 mL) was performed on the aqueous phase, and separately dried. From both extractions yellow oils were obtained. Separately, each oil was dissolved in acetone (50 mL) and HBr 48% (30 mL) was dropwise added and left overnight under stirring. The next day, the precipitate was filtered off, washed with acetone and dried in the rotary evaporator. Acetone caused a lot more precipitate to appear in the filtrate, which was then filtered too, dried and stored separately. The NMR showed both precipitates to be of high purity. From the second extraction at pH 14 was obtained a smaller amount of compound which showed more impurities on the NMR as compared to the first extraction at pH 14 and as a result was not used in the complex synthesis. Highly pure **Me_2tacn·3HBr** was obtained (2.1 g, 5.25 mmol, 25% yield). ^{1}H-NMR (D_2O, 500 MHz, 298 K) δ, ppm: 3.52-3.41 (m, 4H, N-C**H_2**-CH_2), 3.39-3.28 (m, 4H, N-C**H_2**-CH_2), 3.24 (s, 4H, N-C**H_2**-CH_2), 2.80 (s, 6H, N-C**H_3**).

4.3.2. Py$^{(H,H)}$$Me_2$tacn

In a two-neck 100 mL flask fitted for reflux, Py$^{(H,H)}$·HCl (0.248 g, 1.51 mmol) and **Me_2tacn·3HBr** (0.606 g, 1.51 mmol) were added, the flask was purged of air and left under Ar flow. Anhydrous acetonitrile (24 mL, < 100 ppm H_2O) was used to dissolve the solids and anhydrous Na_2CO_3 (1.11 g) and tetrabutylammonium bromide (TBABr, 0.047 g) were mixed as solids. The flask was brought to reflux at 95 °C and stirred under argon for 20 h. Once cooled to room temperature, the mixture was filtered under reduced pressure and the precipitate was washed with CH_2Cl_2. The filtrate was placed in the rotary evaporator and all solvent was removed. To the brown oily residue NaOH (15 mL, 2M) was added and an extraction with CH_2Cl_2 (4 times 40 mL) was performed. After drying on anhydrous $MgSO_4$ and removing the solvent in the rotary evaporator, the oily residue was placed in *n*-hexane (60 mL) and stirred overnight at room temperature. Finally, after filtration and solvent evaporation, **Py$^{(H,H)}$·HCl** presented as a pale yellow liquid (0.221 g, 0.89 mmol, 59% yield). ^{1}H-NMR ($CDCl_3$, 500 MHz, 28K) δ, ppm: 8.54 (ddd, *J* = 4.9, 1.8, 0.9 Hz, **H_6** of py), 7.68 (td, *J* = 7.6, 1.8 Hz, 1H, **H_5** of py), 7.51 (d, *J* = 7.8

Hz, 1H, **H₄** of py), 7.17 (ddd, *J* = 7.5, 4.9, 1.2 Hz, **H₃** of py), 3.87 (s, 2H, C**H₂**-py), 2.90 – 2.78 (m, 8H, N-C**H₂**-CH₂), 2.74 – 2.63 (m, 4H, N-C**H₂**-CH₂), 2.38 (s, 6H, N-C**H₃**).

4.3.3. Py$^{(CN,H)}$Me$_2$tacn

A synthetic route from the available literature[16] was adopted to obtain the ligand 2-((4,7-dimethyl-1,4,7-triazonan-1-yl)methyl)isonicotinonitrile (**Py$^{(CN,H)}$Me$_2$tacn**). It involved the synthesis of the appropriate 4-substituted 2-chloromethyl pyridine as a first step, 2-(chloromethyl)isonicotinonitrile hydrochloride (**Py$^{(CN,H)}$·HCl**).

4.3.3.1. Synthesis of the 2-(chloromethyl)isonicotinonitrile hydrochloride substrate (Py$^{(CN,H)}$·HCl)

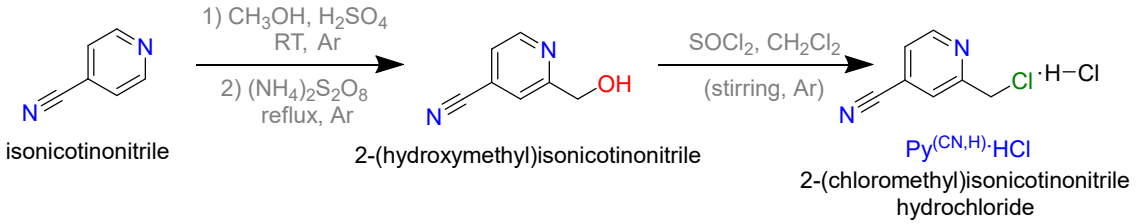

Figure 40. Synthesis of 2-(chloromethyl)isonicotinonitrile hydrochloride (**Py$^{(CN,H)}$·HCl**) starting from isonicotinonitrile.

2-(hydroxymethyl)isonicotinonitrile. In a round bottom flask, isonicotinonitrile (5.51 g, 52.9 mmol) in MeOH (80 mL) was placed under argon and H_2SO_4 (0.5 mL) was dropwise added at room temperature, with stirring. 30 minutes later, ammonium persulfate (19.24 g, 84.3 mmol) dissolved in H_2O (35 mL) was dropwise added. The mixture was refluxed for 1 h in which time a yellow color developed. Once at room temperature the liquid was removed in the rotary evaporator. The pH was adjusted to 9 with a saturated sodium carbonate solution and an extraction with ethyl acetate (AcOEt, 4 times 40 mL) was performed. After drying with anhydrous $MgSO_4$, the solvent was removed under reduced pressure and the obtained solid was purified with silica column chromatography and an eluent composition of 9:1 *n*-hexane:AcOEt to obtain final white **2-(hydroxymethyl)isonicotinonitrile** (1.34 g, 10 mmol, 18.9% yield). ^{1}H-NMR ($CDCl_3$,

500 MHz, 298 K) δ, ppm: 8.78 (m, **H₆** of py), 7.61 (dd, J = 1.6, 0.8 Hz, **H₃** of py), 7.47 (m, **H₅** of py), 4.87 (s, 2H, C**H₂**OH), 3.15 (s, O**H**).

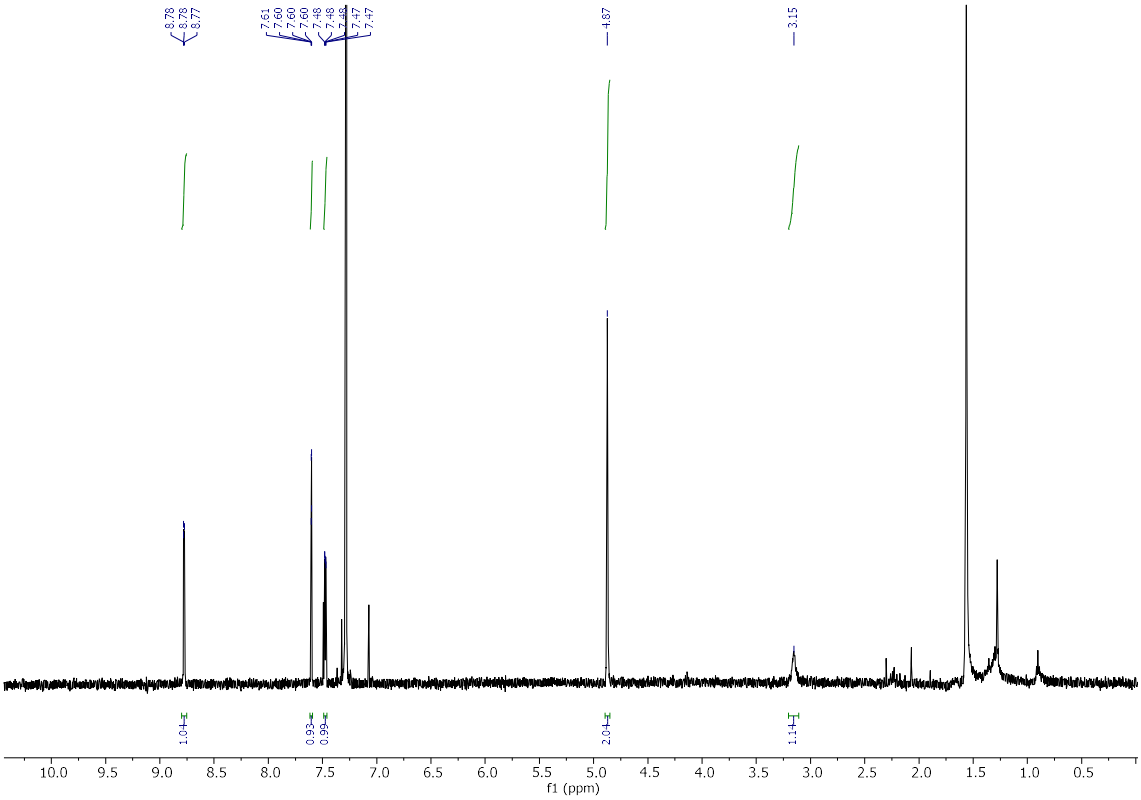

Figure 41. ^{1}H-NMR spectra of **2-(hydroxymethyl)isonicotinonitrile** ($CDCl_3$, 500 MHz, 298 K).

2-(chloromethyl)isonicotinonitrile hydrochloride (Py$^{(CN,H)}$·HCl). To a CH_2Cl_2 solution (35 mL) containing **2-(hydroxymethyl)isonicotinonitrile** (1.34 g, 10 mmol) placed in an ice bath and kept under Ar, thionyl chloride ($SOCl_2$, 2.43 mL, 33.5 mmol) was added dropwise and then left stirring overnight. The next day, all liquid was removed in the rotary evaporator and the solid was washed with diethyl ether (Et_2O) to obtain white solid **Py$^{(CN,H)}$·HCl** (1.44 g, 7.6 mmol, 76% yield). ^{1}H-NMR (CD_3CN, 500 MHz, 298 K) δ, ppm: 8.80 (dd, J = 5.3, 0.9 Hz, **H₆** of py), 8.01 (s, **H₃** of py), 7.84 (dd, J = 5.3, 1.5 Hz, **H₅** of py), 4.90 (s, 2H, C**H₂**Cl). The expected broad signal around 5.50 ppm of N**H** of py is not visible likely due to low traces of H_2O. Due to low scan number and dilute concentration, the **H₆** of py at 8.80 appears as dd instead of d.

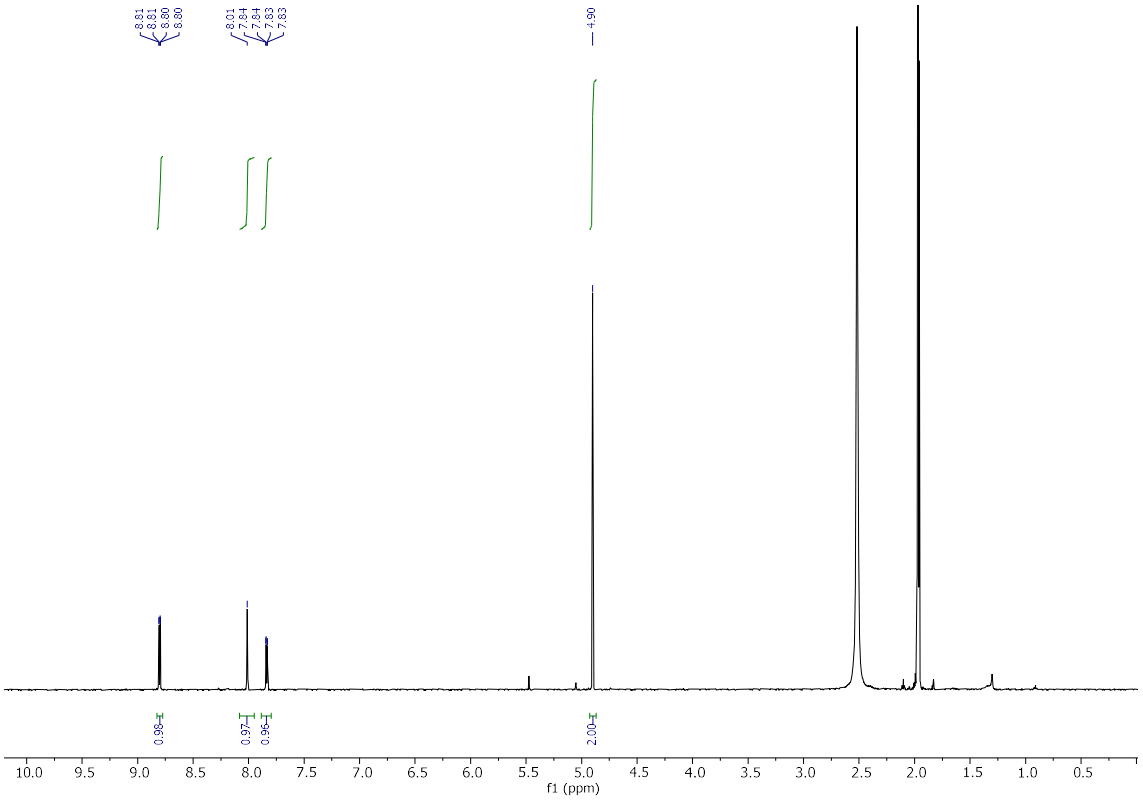

Figure 42. ^{1}H-NMR spectra of 2-(chloromethyl)isonicotinonitrile hydrochloride (**Py$^{(CN,H)}$·HCl**, CD_3CN, 500 MHz, 298 K).

4.3.3.2 Synthesis of the Py$^{(CN,H)}$Me$_2$tacn ligand

Following the synthetic scheme described in **Figure 38**, in a 100 mL two-neck round-bottom flask fitted for reflux **Me$_2$tacn** (0.5 g, 1.25 mmol) and **Py$^{(CN,H)}$·HCl** (0.24 g, 1.25 mmol) were dissolved in CH_3CN (20 mL, < 100 ppm H_2O), under argon. While the solution was kept under Ar, anhydrous Na_2CO_3 (0.95 g) and of tetrabutylammonium bromide (TBABr, 0.04 g) were added as solids, and heated at reflux for 20 h. After that, the mixture was filtered and washed several times with CH_2Cl_2. The filtrate was evaporated in the rotary evaporator and, to the resulting brown residue NaOH (8 mL, 2M) was added, followed by extraction with CH_2Cl_2 (4 times 20 mL). The extract was dried with anhydrous $MgSO_4$ and later the solvent was completely removed. Addition of *n*-hexane (50 mL) and stirring for 12 h followed by filtration (yellow color liquid) and solvent removal, resulted in the desired **Py$^{(CN,H)}$Me$_2$tacn** ligand in the form of an yellow oil (0.159 g, 0.59 mmol, 47% yield). ^{1}H-NMR ($CDCl_3$, 500 MHz, 298 K) δ, ppm: 8.71 (d, *J* = 5.0 Hz, **H$_6$** of py), 7.92 (s, **H$_5$** of py), 7.39 (dd, *J* = 5.0, 1.5 Hz, **H$_3$** of py), 3.94 (s, 2H, C**H$_2$**-

py), 2.89 – 2.85 (m, 4H, N-C**H**$_2$-CH$_2$), 2.77 (s, 4H, CH$_3$-N-C**H**$_3$), 2.72 – 2.66 (m, 4H, N-C**H**$_2$-CH$_2$), 2.40 (s, 6H, N-C**H**$_3$).

4.3.4. Py$^{(COOEt,H)}$Me$_2$tacn

The ethyl 2-((4,7-dimethyl-1,4,7-triazonan-1-yl)methyl)isonicotinate (**Py$^{(COOEt,H)}$Me$_2$tacn**) ligand required the synthesis of the appropriate 4-substituted 2-chloromethyl pyridine substrate.

3.3.4.1. Synthesis of the substrate ethyl 2-(chloromethyl)isonicotinate hydrochloride (Py$^{(COOEt,H)}$·HCl)

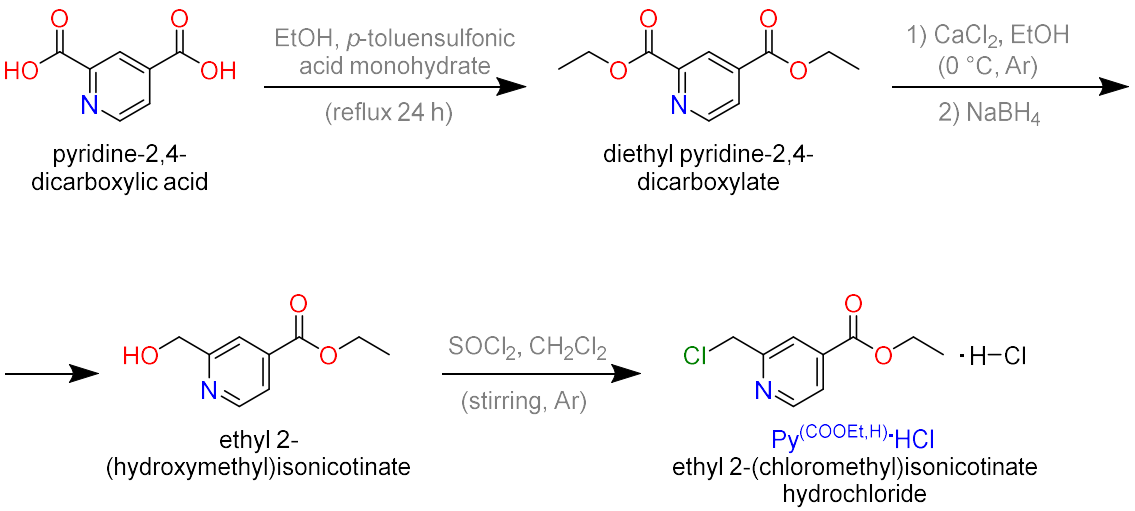

Figure 43. Synthesis of ethyl 2-(chloromethyl)isonicotinate hydrochloride (**Py$^{(COOEt,H)}$·HCl**) starting from pyridine-2,4-dicarboxylic acid.

Diethyl pyridine-2,4-dicarboxylate. A mixture of pyridine-2,4-dicarboxylic acid (5 g, 29.9 mmol) and of *p*-toluenesulfonic acid monohydrate (14 g, 73.6 mmol) in ethanol (350 mL) was refluxed for 24 h after which all solvent was removed under reduced pressure. Chloroform (30 mL) was added to dissolve the residue followed by saturated Na_2CO_3 solution (60 mL) and extracted with chloroform (4 times 60 mL), dried on anhydrous $MgSO_4$ and finally in the rotary evaporator to obtain **diethyl pyridine-2,4-dicarboxylate** (5.5 g, 24.6 mmol, 82.4% yield). ^{1}H-NMR (DMSO, 400 MHz, 298 K) δ, ppm: 8.94 (dd, J = 4.9, 0.9 Hz, **H$_6$** of py), 8.67 (dd, J = 1.6, 0.9 Hz, **H$_3$** of py), 8.05 (dd, J = 4.9, 1.6 Hz, **H$_5$** of

py), 4.51 (dq, J = 32.1, 7.1 Hz, 4H, $CO_2C\mathbf{H_2}CH_3$), 1.47 (dt, J = 16.2, 7.1 Hz, 6H, $CO_2CH_2C\mathbf{H_3}$).

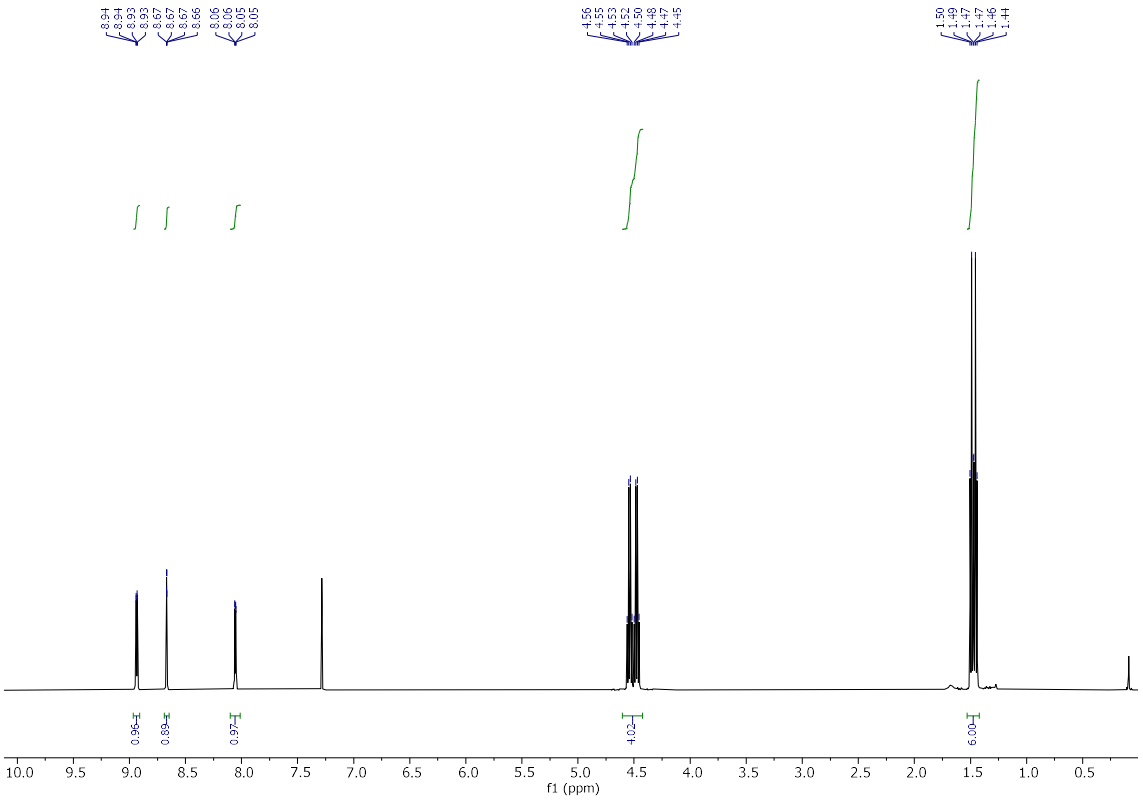

Figure 44. ^{1}H-NMR spectra of **Diethyl pyridine-2,4-dicarboxylate** (DMSO, 400 MHz, 298 K).

Ethyl 2-(hydroxymethyl)isonicotinate. Working under Ar, to a solution of **diethyl pyridine-2,4-dicarboxylate** (1 g, 4.48 mmol) in dry EtOH (9 mL) at 0 °C, crushed anhydrous $CaCl_2$ (0.493 g, 4.44 mmol) was added. While stirring, $NaBH_4$ (0.168 g, 4.44 mmol) was slowly mixed in and the resulting pink mixture was stirred for 4 h at 0 °C, while the completion of the reaction was checked with TLC (with EtOAc:*n*-hexane 1:1 eluent), at which point the reaction was quenched with HCl (0.75 mL, 6M). The white precipitate that appeared was filtered off under reduced pressure and the liquid was evaporated. The resulting residue was passed through a silica column using dry loading and 8:1 EtOAc:*n*-hexane eluent. After drying, **ethyl 2-(hydroxymethyl)isonicotinate** was obtained (0.698 g, 3.85 mmol, 86% yield). ^{1}H-NMR ($CDCl_3$, 400 MHz, 298 K) δ, ppm: 8.74 (s, $\mathbf{H_6}$ of py), 7.88 (s, $\mathbf{H_3}$ of py), 7.82 (s, $\mathbf{H_5}$ of py), 4.89 (s, 2H, $C\mathbf{H_2}OH$), 4.45 (q, J = 7.2 Hz, 2H, $CO_2C\mathbf{H_2}CH_3$), 1.44 (t, J = 7.2 Hz, 3H, $CO_2CH_2C\mathbf{H_3}$). The -O**H** proton (around 3.68)

is not visible in this spectrum. The proper multiplicity of the protons **H_6**, **H_5** and C**H_2**OH (should be doublet instead of singlet) is not visible due to the low scan number used on this spectrum.

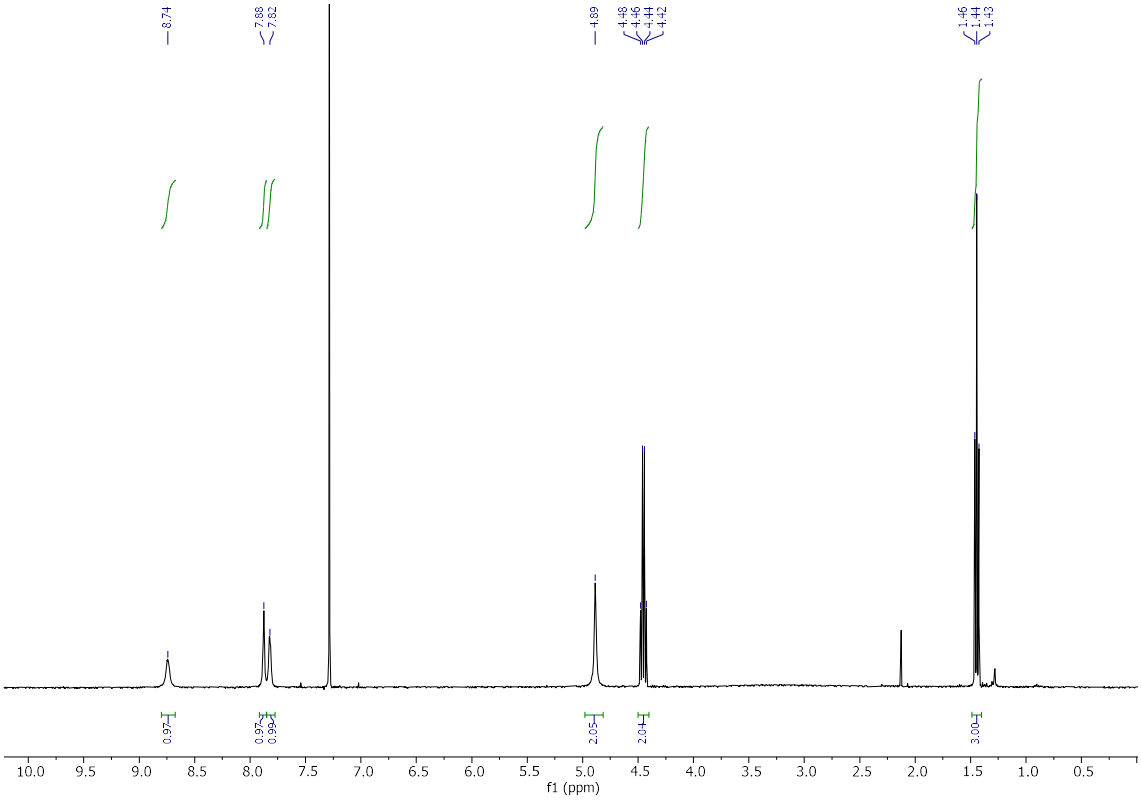

Figure 45. ^{1}H-NMR spectra of **Ethyl 2-(hydroxymethyl)isonicotinate** ($CDCl_3$, 400 MHz, 298 K).

Ethyl 2-(chloromethyl)isonicotinate hydrochloride (Py$^{(COOEt,H)}$·HCl). In a two-neck 50 mL flask fitted with a septa, **ethyl 2-(hydroxymethyl)isonicotinate** (0.698 g, 3.85 mmol) was dissolved in anhydrous CH_2Cl_2 (10 mL). While under Ar flow and at 0 °C, $SOCl_2$ (1 mL) was added dropwise, then left under stirring overnight, at room temperature. Next, the liquids ($SOCl_2$ and $CHCl_3$) were removed via rotary evaporator, and the residue washed several times with Et_2O (100 mL in total) and redried to obtain solid **Py$^{(COOEt,H)}$·HCl** (0.715 g, 3.03 mmol, 79% yield). ^{1}H-NMR ($CDCl_3$, 500 MHz, 298 K) δ, ppm: 8.81 (d, J = 5.6 Hz, **H_6** of py), 8.48 (s, **H_3** of py), 8.27 (dd, J= 5.6 Hz, **H_5** of py), 5.18 (s, 2H, C**H_2**Cl), 4.55 (q, J = 7.2 Hz, 2H, CO_2C**H_2**CH_3), 1.50 (t, J = 7.2 Hz, 3H, CO_2CH_2C**H_3**).

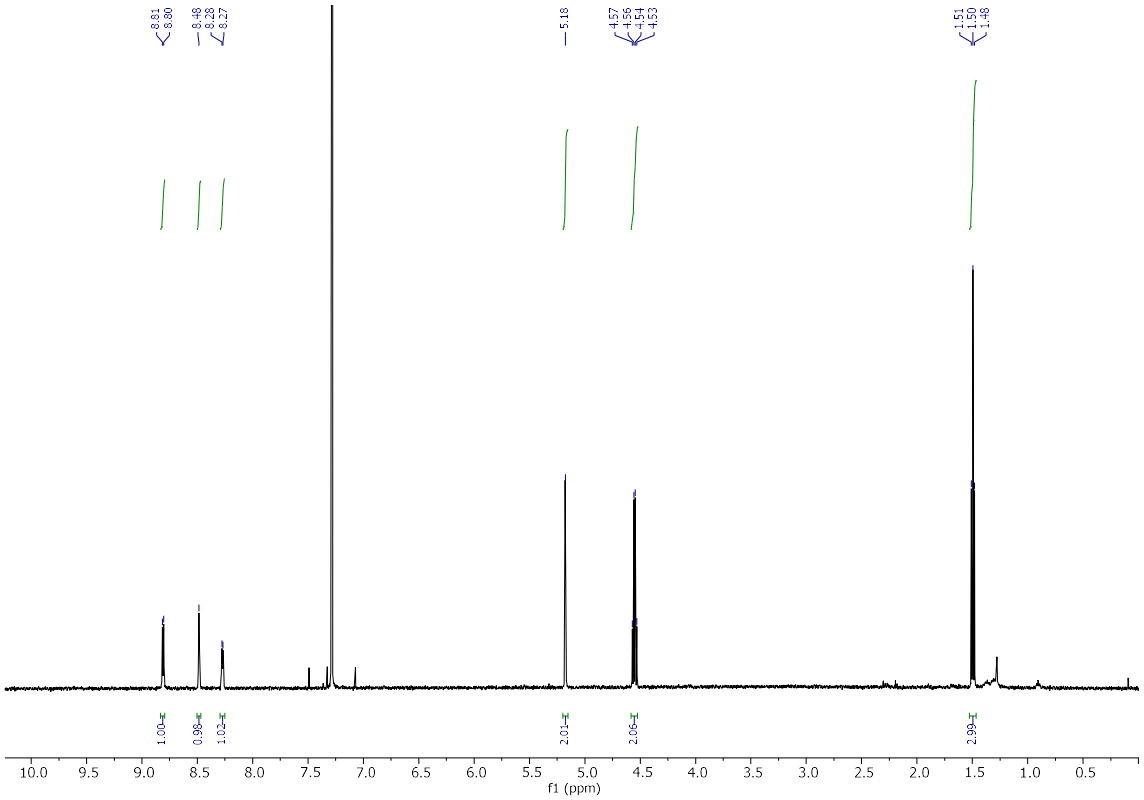

Figure 46. ^{1}H-NMR spectra of ethyl 2-(chloromethyl)isonicotinate hydrochloride (**Py$^{(COOEt,H)}$·HCl**, $CDCl_3$, 500 MHz, 298 K).

4.3.4.2. Synthesis of Py$^{(COOEt,H)}$Me$_2$tacn ligand

Similar to the synthesis of previous ligands (sections **4.3.2. Py$^{(H,H)}$Me2tacn** and **4.3.3. Py$^{(CN,H)}$Me2tacn**), the same conditions were applied starting with **Me$_2$tacn·3HBr** (0.5 g, 1.25 mmol) and **Py$^{(COOEt,H)}$·HCl** (0.295 g, 1.25 mmol) to obtain the **Py$^{(COOEt,H)}$Me$_2$tacn** ligand (0.184 g, 0.58 mmol, 46.4% yield). ^{1}H-NMR ($CDCl_3$, 500 MHz, 298 K) δ, ppm: 8.69 (dd, J = 5.0, 0.9 Hz, **H$_6$** of py), 8.09 (d, J = 0.7 Hz, **H$_5$** of py), 7.72 (dd, J = 5.1, 1.6 Hz, **H$_3$** of py), 4.44 (q, J = 7.1 Hz, 2H, COO-C**H$_2$**-CH$_3$), 3.95 (s, 2H, C**H$_2$**-py), 2.91 – 2.85 (m, 4H, N-C**H$_2$**-CH$_2$), 2.81 (s, 4H, N-C**H$_2$**-CH$_2$), 2.74 – 2.67 (m, 4H, N-C**H$_2$**-CH$_2$), 2.39 (s, 6H, N-C**H$_3$**), 1.44 (t, J = 7.2 Hz, 3H, COO-CH$_2$-C**H$_3$**).

4.3.5. Py$^{(OMe,Me)}$Me$_2$tacn

Using the same procedure as with the previous ligands, **Me$_2$tacn·3HBr** (0.632 g, 1.58 mmol) and **Py$^{(OMe,Me)}$·HCl** (0.351 g, 1.58 mmol) were used to obtain the ligand

Py$^{(COOEt,H)}$Me$_2$tacn (0.257 g, 0.84 mmol, 53.1% yield). ^{1}H-NMR ($CDCl_3$, 500 MHz, 298 K) δ, ppm: 8.17 (s, **H$_6$** of py) 3.78 (s, 3H, O-C**H$_3$**), 3.74 (s, 2H, C**H$_2$**-py), 2.83 – 2.77 (m, 4H, N-C**H$_2$**-CH_2), 2.75 (s, 4H, N-C**H$_2$**-CH_2), 2.67 – 2.62 (m, 4H, N-C**H$_2$**-CH_2), 2.40 (s, 3H, py-C**H$_3$**), 2.33 (s, 6H, N-C**H$_3$**), 2.26 (s, 3H, py-C**H$_3$**).

4.4. Synthesis of complexes

All studied catalysts are highly sensitive to oxygen, and as a result synthetic procedures were carried out inside the glovebox following previously published literature,[16] as described in **Figure 47**, requiring the metal precursor, **Co(OTf)$_2$(CH$_3$CN)$_2$**, to be prepared in advance. All solvents were thoroughly dried and degassed before use.

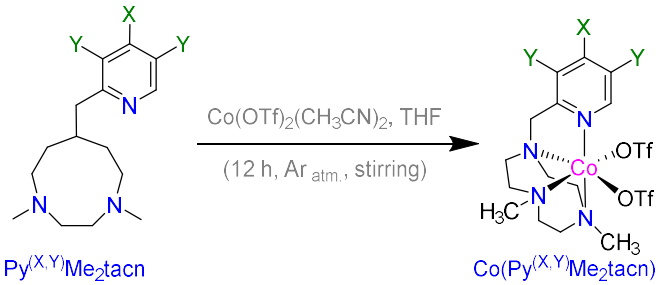

Catalyst	X	Y
Co(Py$^{(H,H)}$Me$_2$tacn)	H	H
Co(Py$^{(CN,H)}$Me$_2$tacn)	CN	H
Co(Py$^{(COOEt,H)}$Me$_2$tacn)	COOEt	H
Co(Py$^{(OMe,Me)}$Me$_2$tacn)	OMe	Me

Figure 47. General synthetic scheme for studied cobalt catalysts.

4.4.1. Co precursor: Co(OTf)$_2$(CH$_3$CN)$_2$

In a Schlenk flask with inert gas atmosphere fitted with drip funnel, $CoCl_2$ (4.95 g, 38 mmol) was dissolved in CH_3CN (30 mL, < 100 ppm H_2O) and trimethylsilyl trifluoromethanesulfonate (Me_3SiOTf, 14.5 mL, 80 mmol) was dropwise mixed in and left stirring at room temperature for 24 h. From the red mixture all solvent was removed, and the resulting solid was redissolved in anhydrous CH_3CN (10 mL). The resulting solution was crystalized in diethyl ether (Et_2O) via slow diffusion. After drying, the resulting **Co(OTf)$_2$(CH$_3$CN)$_2$** presented as pink crystals (8.71 g, 19.8 mmol, 52% yield).

4.4.2 Co(Py$^{(H,H)}$Me$_2$tacn)

In the glovebox, **Py$^{(H,H)}$Me$_2$tacn** (0.221 g, 0.88 mmol) dissolved in tetrahydrofuran (THF, 2 mL) were added dropwise to a stirring solution of **Co(OTf)$_2$(CH$_3$CN)$_2$** (0.391 g, 0.88 mmol) dissolved in THF (2 mL), and were left stirring overnight. The precipitated was decanted and washed 3 times with THF, followed by drying under Ar flow and vacuum. Once dry, the precipitate was dissolved in CH_2Cl_2 (3 mL) and filtrated on Celite. The excess solvent was evaporated under Ar flow, and the resulting solution was allowed to crystallize by slow diffusion of diethyl ether (Et_2O). Finally, red crystalline dry **Co(Py$^{(H,H)}$Me$_2$tacn)** was obtained (0.24 g, 0.39 mmol, 45% yield). ^{1}H-NMR (CD_3CN, 400 MHz, 298 K) δ, ppm: 224.52 (**H$_\alpha$**), 186.82 (C**H$_2$** - tacn), 131.53 (C**H$_2$** - tacn), 102.98 (C**H$_2$** - tacn), 85.16 (**H$_\beta$**), 81.40 (NC**H$_3$**), 61.11 (**H$_{\beta'}$**), 26.48 (**H$_\gamma$**), 22.13.

4.4.3 Co(Py$^{(CN,H)}$Me$_2$tacn)

In a similar manner as with the hydrogen catalyst, from **Py$^{(CN,H)}$Me$_2$tacn** (0.159 g, 0.58 mmol) and **Co(OTf)$_2$(CH$_3$CN)$_2$** (0.26 g, 0.59 mmol), the catalyst **Co(Py$^{(CN,H)}$Me$_2$tacn)** was obtained (0.23 g, 0.36 mmol, 63% yield). ^{1}H-NMR (CD_3CN, 400 MHz, 298 K) δ, ppm: 212.70 (**H$_\alpha$**), 186.21, 145.79, 141.02, 94.56, 78.36 (NC**H$_3$**), 75.71(**H$_\beta$**), 54.62 (**H$_{\beta'}$**), 19.46.

4.4.4 Co(Py$^{(COOEt,H)}$Me$_2$tacn)

Using the same procedure as with the previous catalysts, **Py$^{(COOEt,H)}$Me$_2$tacn** (0.184 g, 0.57 mmol) and **Co(OTf)$_2$(CH$_3$CN)$_2$** (0.26 g, 0.59 mmol) were used to synthesize **Co(Py$^{(COOEt,H)}$Me$_2$tacn)** (0.237 g, 0.35 mmol, 61.4% yield). ^{1}H-NMR (CD_3CN, 400 MHz, 298 K) δ, ppm: 215.38 (**H$_\alpha$**), 185.06 (C**H$_2$** - tacn), 140.77 (C**H$_2$** - tacn), 135.77 (C**H$_2$** - tacn), 97.22, 79.95 (**H$_\beta$** + NC**H$_3$**), 57.80 (**H$_{\beta'}$**), 20.64, 8.19 (COOC**H$_2$**CH_3), 4.41 (COOCH_2C**H$_3$**).

4.4.5 Co(Py$^{(OMe,Me)}$Me$_2$tacn)

Starting with **Py$^{(OMe,Me)}$Me$_2$tacn** (0.234 g, 0.84 mmol) and **Co(OTf)$_2$(CH$_3$CN)$_2$** (0.371 g) and following the same synthetic procedure as with all previous catalysts, red **Co(Py$^{(OMe,Me)}$Me$_2$tacn** was obtained (0.262 g, 0.39 mmol, 47% yield). ^{1}H-NMR (CD_3CN, 400 MHz, 298 K) δ, ppm: 232.53 (**H$_\alpha$**), 183.55 (C**H$_2$** - tacn), 123.38 (C**H$_2$** - tacn), 109.47 (C**H$_2$** - tacn), 85.04 (NC**H$_3$**), 25.77 (Py-C**H$_3$**), 13.62 (Py-C**H$_3$**), 7.30 (O-C**H$_3$**).

5. Conclusion

Cobalt complexes with different electron-donating or electron-withdrawing groups **Co(Py$^{(H,H)}$Me$_2$tacn), Co(Py$^{(CN,H)}$Me$_2$tacn), Co(Py$^{(COOEt,H)}$Me$_2$tacn), Co(Py$^{(OMe,Me)}$Me$_2$tacn)** were successfully synthesized.

CV experiments under argon and under CO_2 have been performed and an anodic shift in the first reduction wave ($Co^{II/I}$ transition) for the hydrogen and dimethyl methoxy catalyst has been observed. For the cyan and ester catalysts no such shift was noticed. The comparison between argon and CO_2 at the second reduction wave showed an increase in current for the hydrogen, ester and dimethyl methoxy catalysts corresponding to enhanced interaction between $Co^{I/0}$ species and CO_2, however for the ester no defined peak was observed without the addition of MeOH. For the cyan catalysts, the one with the strongest electronic-withdrawing effect, without MeOH even the increase in current was not observed under the same conditions.

Titrations with MeOH revealed clear current increases with the increase in MeOH concentration, and a working MeOH concentration of 3.53 M was chosen to provide all catalysts with suitable conditions for a comparative study, where they all display an appreciable activity.

CPE experiments were conducted under dark over 120 minutes (90 minutes in the case of the cyan catalyst) with regular 5-minute interval measurements of the produced gas via GC chromatography. The results were used to calculate Faraday efficiencies and turnover numbers for each catalyst. A direct correlation between the electron-withdrawing strength of the substituents in the ligand and FE was observed, with the cyan catalyst having FE_{CO} of 51%, the ester 39%, the hydrogen 19% and lastly the dimethyl methoxy catalyst only 6% FE_{CO}. **Co(Py$^{(OMe,Me)}$Me$_2$tacn)** showed very high FE for hydrogen evolution instead, at 55%. A similar correlation in TON, however, was not observed.

Light-assisted CPE experiments performed under irradiation at 447 nm showed little improvement in the catalytic activities of **Co(Py$^{(CN,H)}$Me$_2$tacn)** and **Co(Py$^{(COOEt,H)}$Me$_2$tacn),** and a more substantial impact for **Co(Py$^{(H,H)}$Me$_2$tacn)** and especially for **Co(Py$^{(OMe,Me)}$Me$_2$tacn).** The electron-withdrawing effect of the cyan and ester moieties allowed the complexes to perform similarly in dark as well as light, while the electron-donating analogues benefitted from the presence of light irradiation.

6. Acknowledgements

I would like to express my sincere gratitude to my supervisor, Prof. Julio Lloret-Fillol, for the opportunity to work in his research group and learn from his expertise and way of thinking. I would like to thank all members of the hosting research group for their continued help, and I am particularly grateful to Mattia Vettori for his daily support throughout my work. His willingness to answer my questions, troubleshoot experimental issues, and share his expertise with data analysis greatly accelerated my progress. I would also like to thank the institute ICIQ for providing access to their advanced facilities and for their welcoming attitude. I am also deeply thankful to Prof. Josep M. Ricart Pla for his unwavering friendship and ever-present help in all matters, academic and otherwise. His constant encouragement was a source of strength throughout my thesis journey.

7. References

(1) Rae, J. W. B.; Zhang, Y. G.; Liu, X.; Foster, G. L.; Stoll, H. M.; Whiteford, R. D. M. Atmospheric Cobinf2einf over the Past 66 Million Years from Marine Archives. *Annu Rev Earth Planet Sci* **2021**, *49* (Volume 49, 2021), 609–641. https://doi.org/10.1146/ANNUREV-EARTH-082420-063026/1.

(2) Liu, Z.; Deng, Z.; Davis, S.; Ciais, P. Monitoring Global Carbon Emissions in 2022. *Nature Reviews Earth & Environment 2023 4:4* **2023**, *4* (4), 205–206. https://doi.org/10.1038/s43017-023-00406-z.

(3) Liu, Z.; Deng, Z.; Davis, S. J.; Ciais, P. Global Carbon Emissions in 2023. *Nature Reviews Earth & Environment 2024 5:4* **2024**, *5* (4), 253–254. https://doi.org/10.1038/s43017-024-00532-2.

(4) Hassan, Q.; Algburi, S.; Sameen, A. Z.; Al-Musawi, T. J.; Al-Jiboory, A. K.; Salman, H. M.; Ali, B. M.; Jaszczur, M. A Comprehensive Review of International Renewable Energy Growth. *Energy and Built Environment* **2024**. https://doi.org/10.1016/J.ENBENV.2023.12.002.

(5) Fang, S.; Rahaman, M.; Bharti, J.; Reisner, E.; Robert, M.; Ozin, G. A.; Hu, Y. H. Photocatalytic CO2 Reduction. *Nature Reviews Methods Primers 2023 3:1* **2023**, *3* (1), 1–21. https://doi.org/10.1038/s43586-023-00243-w.

(6) Saha, P.; Amanullah, S.; Dey, A. Selectivity in Electrochemical CO2Reduction. *Acc Chem Res* **2022**, *55* (2), 134–144. https://doi.org/10.1021/ACS.ACCOUNTS.1C00678/ASSET/IMAGES/MEDIUM/AR1C00678_0014.GIF.

(7) Usman, M.; Humayun, M.; Garba, M. D.; Ullah, L.; Zeb, Z.; Helal, A.; Suliman, M. H.; Alfaifi, B. Y.; Iqbal, N.; Abdinejad, M.; Tahir, A. A.; Ullah, H. Electrochemical Reduction of CO2: A Review of Cobalt Based Catalysts for Carbon Dioxide Conversion to Fuels. *Nanomaterials 2021, Vol. 11, Page 2029* **2021**, *11* (8), 2029. https://doi.org/10.3390/NANO11082029.

(8) Yaseen, M.; Humayun, M.; Khan, A.; Usman, M.; Ullah, H.; Tahir, A. A.; Ullah, H. Preparation, Functionalization, Modification, and Applications of Nanostructured Gold: A Critical Review. *Energies 2021, Vol. 14, Page 1278* **2021**, *14* (5), 1278. https://doi.org/10.3390/EN14051278.

(9) Wang, J. W.; Huang, H. H.; Sun, J. K.; Ouyang, T.; Zhong, D. C.; Lu, T. B. Electrocatalytic and Photocatalytic Reduction of CO2 to CO by Cobalt(II) Tripodal Complexes: Low Overpotentials, High Efficiency and Selectivity. *ChemSusChem* **2018**, *11* (6), 1025–1031. https://doi.org/10.1002/CSSC.201702280.

(10) Cometto, C.; Chen, L.; Lo, P. K.; Guo, Z.; Lau, K. C.; Anxolabéhère-Mallart, E.; Fave, C.; Lau, T. C.; Robert, M. Highly Selective Molecular Catalysts for the CO2-to-CO Electrochemical Conversion at Very Low Overpotential. Contrasting Fe vs Co Quaterpyridine Complexes upon Mechanistic Studies. *ACS Catal* **2018**, *8* (4), 3411–3417.

https://doi.org/10.1021/ACSCATAL.7B04412/ASSET/IMAGES/LARGE/CS-2017-044125_0004.JPEG.

(11) Elgrishi, N.; Chambers, M. B.; Fontecave, M. Turning It off! Disfavouring Hydrogen Evolution to Enhance Selectivity for CO Production during Homogeneous CO2 Reduction by Cobalt–Terpyridine Complexes. *Chem Sci* **2015**, *6* (4), 2522–2531. https://doi.org/10.1039/C4SC03766A.

(12) Lacy, D. C.; McCrory, C. C. L.; Peters, J. C. Studies of Cobalt-Mediated Electrocatalytic CO2 Reduction Using a Redox-Active Ligand. *Inorg Chem* **2014**, *53* (10), 4980–4988. https://doi.org/10.1021/IC403122J/SUPPL_FILE/IC403122J_SI_002.PDF.

(13) Fisher, B.; Eisenberg, R. Electrocatalytic Reduction of Carbon Dioxide by Using Macrocycles of Nickel and Cobalt. *J Am Chem Soc* **1980**, *102* (24), 7361–7363. https://doi.org/10.1021/JA00544A035/ASSET/JA00544A035.FP.PNG_V03.

(14) Shimoda, T.; Morishima, T.; Kodama, K.; Hirose, T.; Polyansky, D. E.; Manbeck, G. F.; Muckerman, J. T.; Fujita, E. Photocatalytic CO2 Reduction by Trigonal-Bipyramidal Cobalt(II) Polypyridyl Complexes: The Nature of Cobalt(I) and Cobalt(0) Complexes upon Their Reactions with CO2, CO, or Proton. *Inorg Chem* **2018**, *57* (9), 5486–5498. https://doi.org/10.1021/ACS.INORGCHEM.8B00433.

(15) Fernández, S.; Franco, F.; Casadevall, C.; Martin-Diaconescu, V.; Luis, J. M.; Lloret-Fillol, J. A Unified Electro- And Photocatalytic CO2 to CO Reduction Mechanism with Aminopyridine Cobalt Complexes. *J Am Chem Soc* **2020**, *142* (1), 120–133. https://doi.org/10.1021/JACS.9B06633/SUPPL_FILE/JA9B06633_SI_003.PDF.

(16) Call, A.; Franco, F.; Kandoth, N.; Fernández, S.; González-Béjar, M.; Pérez-Prieto, J.; Luis, J. M.; Lloret-Fillol, J. Understanding Light-Driven H2 Evolution through the Electronic Tuning of Aminopyridine Cobalt Complexes. *Chem Sci* **2018**, *9* (9), 2609–2619. https://doi.org/10.1039/C7SC04328G.